Theory, Instrumentation, and Applications of Electron Paramagnetic Resonance Oximetry

Rizwan Ahmad and Periannan Kuppusamy*

Center for Biomedical EPR Spectroscopy and Imaging, Davis Heart and Lung Research Institute, Department of Internal Medicine, The Ohio State University, Columbus, Ohio 43210

Received December 8, 2009

Contents

* To whom correspondence should be addressed. E-mail: kuppusamy.1@osu.edu.

1. Introduction

Oxygen is the third most abundant element in the universe by mass after hydrogen and helium. It has an atomic number of 8 and is represented by the symbol O. At standard temperature and pressure, two atoms of the element bind to form molecular oxygen (O_2), which is a colorless, odorless, and tasteless diatomic gas, occupying 20.9% of air volume. Since its discovery[1] in the 1770s, its properties, chemistry, and relevance to life have intrigued generations of scholars and scientists. A multitude of scientific evidence[2−4] builds a compelling case for the vital role of oxygen in the evolution of life on earth. Aerobic organisms consume molecular oxygen to generate chemical energy, required for biologic processes, in the form of adenine triphosphate. Also, O_2 serves as a regulatory molecule for important physiologic processes.

In mammals, including humans, inhaled oxygen from the lungs is carried to the target tissue by the oxygen-carrying protein, hemoglobin. At the target tissue, where the cells actively engage themselves in respiration (oxidative phosphorylation), oxygen is released from the oxygen-bound hemoglobin (oxyhemoglobin), and the released oxygen is

10.1021/cr900396q
Published on Web 03/10/2010

Rizwan Ahmad received a B.S. degree with honors in electrical engineering from The University of Engineering and Technology, Lahore, Pakistan, in 2000, and M.S. and Ph.D. degrees in electrical and computer engineering from The Ohio State University in 2004 and 2007, respectively. In his M.S., he worked as a research assistant on electrical capacitance tomography with the Department of Chemical Engineering. In his Ph.D., he worked as a research assistant on fast data collection and reconstruction methods for EPR imaging with the Davis Heart & Lung Research Institute (DHLRI). Since 2007, he has been with the DHLRI, Ohio State University Medical Center, Columbus, Ohio, where he is currently appointed as a Research Scientist. His research interests include biomedical signal processing, tomographic reconstruction, in vivo oximetry, and EPR spectroscopy and imaging.

Periannan Kuppusamy received his Ph.D. degree in 1986 with specialization in EPR spectroscopy from the Indian Institute of Technology, Chennai, India. Following a brief Fogarty Fellowship program at the National Institutes of Health (NIH), Dr. Kuppusamy joined the Johns Hopkins University School of Medicine in 1987 as a Research Fellow and became a faculty in the cardiology division in 1991. In 2002, Dr. Kuppusamy moved to The Ohio State University, where he is currently a Professor in the Department of Internal Medicine. Dr. Kuppusamy functions as the Director of the Center for Biomedical Spectroscopy & Imaging and Director of the Small Animal Imaging Center in the OSU College of Medicine. Dr. Kuppusamy has developed a variety of in vivo EPR spectroscopic and imaging techniques for noninvasive measurements of free radicals and oxygen in biological systems. His major research focus is stem cell therapy for myocardial infarction, novel bifunctional therapeutics for cardiovascular and cancer applications, and technology development for EPR-based oximetry for clinical applications. Dr. Kuppusamy has published over 280 peer-reviewed manuscripts of his research in leading scientific journals. He has several grants from the National Institutes of Health for the development of clinical oximetry and cardiovascular research. Dr. Kuppusamy has received research awards, including a Silver Medal in 2006 from the International EPR Society, for significant contributions to the development of EPR imaging for biomedical applications and a Doctorate of Medicine (honoris causa) in 2008 from the University of Pecs (Pecs, Hungary) for his cardiovascular research.

available to the metabolically active tissues. Any imbalance in tissue oxygen levels, which may occur due to altered supply or utilization of oxygen, may affect metabolic homeostasis and lead to pathophysiological conditions.[5] In addition, the level of oxygen at specific sites may affect cell signaling.[6,7] Hence, a precise knowledge of the levels of oxygen in the tissue of interest will be of paramount importance in our ability to understand the mechanism of pathogenesis and to develop strategies to correct the imbalance. This would require methods capable of quantifying the levels of tissue oxygenation with good spatial and temporal resolution. The information gained will enable better understanding of various metabolic and disease states and will assist in making effective clinical decisions regarding treatment and therapy options. The chemical and physical properties of oxygen enable a wide variety of methods for measuring and mapping oxygen content in vivo.

There are numerous reviews on various oxygen measurement techniques and their applications to specific organs and diseases.[8−10] For any particular application, the choice of an oximetry method is determined by its accuracy, measurement procedure, acquisition time, invasiveness, and relevance of the measured form of oxygen, which includes oxygen concentration, partial pressure of oxygen (pO_2), and oxygen saturation.

Electron paramagnetic resonance (EPR), also called electron spin resonance, is a magnetic resonance-based technique capable of measuring oxygen levels in biological sampling, both in vitro and in vivo.[11] Over the past couple of decades, the EPR oximetry technique has been continually refined to collect repetitive, minimally invasive, and accurate measurements of pO_2 over an extended duration.[12,13] At the same time, the biological applications for EPR oximetry have been rapidly growing and now include monitoring of tumor oxygenation for the determination of cancer treatment efficacy[14,15] and measuring of tissue oxygen levels for the estimation of the extent of myocardial injury during both ischemia and subsequent reperfusion.[16]

This review provides a brief survey of the basic principles and novelty, instrumentation, measurement procedures, and a few promising applications of EPR oximetry for biological systems. Section 2 describes some commonly used experimental and clinical methods for tissue oxygen measurements. Section 3 discusses the basic principle of EPR oximetry and provides motivation by outlining its unique advantages. Section 4 provides the basic layout of a typical EPR spectrometer. Section 5 covers basics of data collection and processing procedures for EPR oximetry and highlights some of the developments proposed to speed up the acquisition process. Section 6 describes spin probe development for EPR oximetry and encapsulation methods for particulate spin probes. Section 7 lists a few important, mainly in vivo, applications of EPR oximetry.

2. History of Tissue Oxygen Measurement

Even though the discovery of oxygen was made in the late 18th century, measurements of oxygen levels in biological samples have been studied only in the 20th century. In the 1930s, the German scientist Karl Matthes first used variable transmission of red and infrared light through the human ear to assess oxygenation.[17] An ear oximeter, developed in 1942 by the American scientist Glen Milliken, was used for many years in pulmonary and physiology laboratories. Several other attempts were made in the 1960s,[18,19] but it was in the late 1980s that the computerized polarographic needle electrode system was used to assess tumor oxygenation in the clinic.[20] The use of this electrode technique helped establish the role of hypoxia in determining

the effectiveness of radio- or chemotherapy.[21,22] Now, there exist several oximetry methods that are based on other principles, including fluorescence and phosphorescence quenching, optical detection, immunohistochemical detection, and magnetic resonance techniques.

2.1. Chemical Methods

2.1.1. Polarographic Electrode

Blood and tissue oximetry using a polarographic electrode was proposed by Leland Clark.[23] The method is based on measuring the electric current resulting from the electrochemical reduction of oxygen at the cathode. In addition to the consumption of oxygen, the relatively large size of earlier designs lead to serious practical issues, such as artifacts due to blood flow, acute tissue injury, and signal averaging over a large volume. To avoid such issues, efforts have been made to design miniaturized polarographic electrodes,[24] also called "microelectrodes". Modern recessed tip microelectrodes are available in the range of 5−10 μm[25] in diameter.

The commercially available recessed tip microelectrode by Eppendorf has been widely used to measure in vivo oxygenation of tissues. Because of the widespread use of this technique, it has been considered the "gold standard" for measuring tissue oxygenation.[26] The method has been extensively used for measuring oxygen in tumor[27−29] and brain.[30] However, there are several disadvantages associated with polarographic electrodes including consumption of oxygen by the electrode, poor signal-to-noise ratio (SNR) at low oxygen concentrations, inability to make repeated measurements, and the highly invasive nature of the measurement procedure.

2.1.2. Transcutaneous Oxygen Sensor

A different setup using polarographic oxygen electrodes has been used for transcutaneous oxygen monitoring[31] (TCOM). In a typical setup, the electrode is pressed against skin to effectively measure the diffusion of oxygen through skin noninvasively. The method is quantitative, and it is thus far the only device that measures oxygen delivery to an end organ (the skin). It has been used to monitor oxygenation levels (in mmHg) in the skin, especially for premature infants[32] but also for adults in the intensive care setting.[33] Physicians also use TCOM to determine whether or not there is adequate blood flow to support healing of a lower extremity wound,[34] such as a venous stasis ulcer or diabetic foot ulcer. The necessity for exogenous skin heating along with the sensitivity of this method to skin properties, temperature fluctuations, and mechanical pressure pose a serious limit to it accuracy.

2.1.3. Immunochemical Methods

This technique requires the administration of a hypoxia marker such as 2-nitroimidazoles.[35] These bioreductive markers belong to the class of compounds that have maximum binding to severely hypoxic cells (with less than 0.38 mmHg of oxygen, for example) and increased inhibition to increasing oxygenation as dictated by Michaelis−Menten kinetics.[36] This approach is also used in combination with immunohistochemical techniques where hypoxia can be visualized and compared with necrosis, proliferation, or oxygen-regulated protein expression.[37] However, the dependence of hypoxia marker binding on factors other than pO_2, such as level of tissue perfusion or the amount of reductases in the tissue, may make quantification of the results more complex. Also, binding of the hypoxia marker may not differentiate between long-term steady-state hypoxia and short-term transient hypoxia.

2.2. Optical Methods

2.2.1. Fluorescence Oximetry

Fluorescence oximetry is based on oxygen-dependent changes in the lifetime of fluorescence. This principle has been used in the construction of OxyLite,[38] a widely used commercially available oxygen-measuring sensor. It uses ruthenium chloride, a fluorescent dye, connected to the tip of a fiber optic cable. Photodiodes excite the fluorophores of the dye, and the resulting fluorescence lifetime relates inversely to the oxygen tension at the tip. A typical probe diameter is ~220 μm.

This method does not consume oxygen and is capable of monitoring rapid temporal oxygen changes at a given tissue location. This technique has been widely used for the measurement of oxygen in tumor,[39] liver, and brain[40] and has been compared to other oximetry techniques.[41,42] Some drawbacks of the technique include sensitivity to movement and temperature, pressure-induced artifacts due to insertion of the probe, invasiveness, and the inability to perform repeated measurements at the same location overtime.

2.2.2. Phosphorescence Oximetry

The measurement of oxygen using phosphorescence oximetry involves injection of a phosphor material into the vasculature and measurement of the oxygen-induced changes in the lifetime of the induced phosphorescence.[43] A bifurcated light guide is used to focus the excitation light from the source to the surface of the tissue where it is detected by a phosphorometer. Oximetry by phosphorescence quenching has now been in use for over two decades.[44] This technique is gaining importance for in vivo applications[45,46] as further technical improvements, including probe development,[47] are continuously being made. In a typical setup, the phosphorometer (detector) utilizes photomultipliers or avalanche photodiodes to measure the phosphorescence signal to get information about the distribution of the lifetimes and the amplitudes of the phosphor probe. Data analysis involving calibration and deconvolution subsequently gives histogram representations of pO_2 over the sampled region. When the measurements are done in a grid pattern, it is possible to construct contour maps, which then can be used to compute the volume fraction of tissue sampled for any selected range of pO_2 values. Besides the minimally invasive nature, a significant advantage of this method is its ability to provide real-time, repeated measurements. Phosphorescence oximetry has been widely used for mapping the oxygen distribution in the retina[48] and other organs such as the heart and brain.[49] It has also been used to study oxygen distribution in murine vasculature[50] and oxygenation of tumors.[51] A major disadvantage of this technique is the need to inject the phosphor material into the vasculature. Also, the technique provides only the vascular oxygen concentration.

2.2.3. Pulse Oximetry

Pulse oximetry enables measurement of oxygen saturation of blood, which indicates the balance between oxygen

delivery and consumption. It is a noninvasive method based on the differential absorption of red and infrared light by oxyhemoglobin and deoxyhemoglobin.[52] The ratio of the absorption of the red and infrared light is converted to the ratio of oxyhemoglobin and deoxyhemoglobin. The pulse oximeter consists of a pair of small light-emitting diodes, one red and one infrared, facing a photodetector. Sites of measurement include fingers, toes, and earlobes, which have adequate blood flow. Because of the noninvasive nature and ease of use, this technique is more commonly used for clinical applications.[53] The major shortcomings of this method include requirement of adequate arterial perfusion, motion artifacts, inability to measure tissue oxygenation, measurement of oxygen saturation rather than the actual oxygen content, inability to distinguish between carboxyhemoglobin and oxyhemoglobin, and stray light interference.

2.2.4. Near-Infrared Spectroscopy (NIRS)

The NIRS technique works on a physical principle similar to that of pulse oximetry, that is, the light transmitted through a tissue is absorbed differently by oxygenated and deoxygenated hemoglobin in the circulation. The NIRS technique is noninvasive, with excellent temporal resolution, low cost, and portability.[54] Because of the longer penetration depth of NIRS, real-time repeated measurements from relatively deep locations are possible. NIRS has been used for clinical studies of oxygen utilization in tissues and muscle oxygenation,[55] especially in the area of exercise physiology. In other clinical studies, NIRS has been used for monitoring of peripheral vascular disease,[56] ischemic and hemorrhagic stroke,[57] cerebral oxygenation,[58] and blood flow measurements.[59] One drawback of the NIRS method is that it does not measure tissue pO_2 directly but rather provides the information about vascular oxygen saturation. Also, the absorption spectra of most common chromophores, such as oxyhemoglobin, deoxyhemoglobin, and cytochrome *c* oxidase, overlap, which may result in ambiguous quantification.[60]

2.2.5. Hyperspectral Imaging (HSI)

Oximetry using HSI relies on analyzing reflectance measurements that are backscattered and spectrally altered by the tissue to assess blood oxygen saturation.[61] The working principle of HSI is similar to NIRS, but unlike NIRS, it collects and processes information from many different visible wavelengths. The main advantage of using this technique is that it is noninvasive and allows a direct observation of blood oxygen supply. This method has been applied to measure oxygen saturation in the optical nerve head and retina.[62] It has also been used to evaluate hemoglobin saturation in murine tumors[63] and tissue perfusion in humans.[64] In addition, HSI-based methods have been used to investigate wound healing[65] and to diagnose hemorrhagic shock.[66] Major drawbacks associated with HSI include lack of accuracy, complexity of data analysis, and inability to directly measure tissue oxygenation.

2.3. Nuclear and Magnetic Methods

2.3.1. Positron Emission Tomography (PET) Imaging

PET-based oximetry uses short-lived positron-emitting radionuclides for in vivo imaging of a variety of hypoxia biomarkers.[67] Besides radiolabeling of the biomarkers, the basic principle of this modality is similar to that of immunochemical methods. The common hypoxia markers used in PET are ^{18}F-containing imidazoles[68] (e.g., ^{18}F fluoromisonidazole) and ^{18}F-containing pentafluorinated derivative of etanidazole.[69] Researchers at Washington University and Searle Radiographers developed instrumentation that could be used for in vivo imaging of the positron-emitting radionuclides.[70] PET oximetry is a noninvasive method that has been extensively used in tumor models for hypoxia mapping in mice and rat. Clinical studies include head and neck cancer[71] and lung cancer.[72] The PET/magnetic resonance imaging (MRI) and PET/computed tomography (CT) combined modalities are also gaining importance as they have the added advantage of obtaining anatomical information along with PET data. The use of PET oximetry is limited by the availability and cost of cyclotrons needed to produce short-lived radionuclides.

2.3.2. ^{19}F MRI

In 1988, Busse et al.[73] showed that ^{19}F nuclear magnetic resonance (NMR) spin−lattice relaxation rate (R1) of perfluorocarbon (PFC) probes could be used for imaging tumor pO_2 in vivo. The technique is based on NMR, but unlike conventional MRI (proton imaging), a probe based on PFCs is used. The PFCs are infused intravenously in the form of emulsions.[74] The ^{19}F spin−lattice relaxation rate (R1) of PFCs varies linearly with dissolved oxygen concentration. Thus, the ^{19}F-based oximetry reports absolute values of oxygen concentration. Hexafluorobenzene[75] (HFB) and perfluoro-15-crown-5-ether[76] have been the most widely used PFCs for this application. Using this technique, it is possible to image pO_2 as well as to follow dynamic changes in tumor oxygenation. It is also possible to combine the ^{19}F images and ^{1}H anatomical images to provide spatial registration. This method has been used in rodent models for different types of tumors including breast[77] and prostate.[78] Studies have also been conducted in rat brain,[79] lung,[80] and human eye.[81] Yu et al.[82] have reviewed ^{19}F MRI for physiological and pharmacological applications. The main concern with ^{19}F MRI is the toxicity of PFCs, which needs to be fully characterized before this method can be used for clinical applications.

2.3.3. Blood Oxygen Level-Dependent (BOLD) Imaging

In 1982, Thulborn et al.[83] described the oxygenation dependence of the transverse relaxation time of water protons. Later, Ogawa et al. described BOLD MRI of tissues for imaging the blood oxygen level in rat brain.[84] BOLD images reflect the changes in the amount of oxygen bound to hemoglobin in blood. The presence of deoxyhemoglobin, which is paramagnetic in nature, can cause differences in susceptibility (i.e., changes in the local magnetic field) around the blood vessels, which affects the relaxation properties of the surrounding protons. Thus, a change in the T_2-weighted image can be used to quantify changes in blood oxygenation. BOLD MRI oximetry is noninvasive and can be performed using available clinical scanners and has the advantage of the availability of fast imaging sequences. It can also provide information regarding temporal changes[85] in oxygenation. The repeatability and voxel-by-voxel information about changes in blood oxygenation coregistered with anatomical information are also advantages over other imaging techniques. A major disadvantage of the BOLD oximetry is that

it does not provide quantitative information[86] of blood oxygenation. It measures the changes in blood oxygenation but not absolute oxygen concentration in tissue.

3. EPR Oximetry

EPR oximetry is a minimally invasive magnetic resonance method capable of measuring direct and absolute values of pO_2 or O_2 concentrations. In 1977, Backer et al.[87] reported the reversible and repeatable effect of oxygen concentration on the superhyperfine structure of EPR spectra of a soluble spin probe, also called spin label. Soon after, more oxygen-sensitive spin probes were developed and used for biological applications.[88,89] In the 1980s, James Hyde explored the quantifiable affect of oxygen concentration on the relaxation rates[90,91] of various spin probes, which remains the basis of present day EPR oximetry. He also greatly contributed to the development of instrumentation[92] and methodology for making EPR measurements. In 1986, Subczynski et al. reported the first in vivo EPR oximetry measurement,[93] which was conducted on mice using an L-band EPR spectrometer. Over the last two decades, EPR oximetry has emerged as a promising technique for biological applications with unique advantages over other existing oximetry methods.[11,94] It possesses a high sensitivity to pO_2 and can provide three-dimensional (3D) mapping of oxygen distribution, if required. This method shows a high specificity because of minimal interference from other sources. In addition, the spin probes are nontoxic and are generally stable in a tissue environment. In fact, particulate (solid-state, crystalline, and water-insoluble) spin probes can stay in a biological sample for months without losing their oxygen sensitivity.[95,96] Therefore, the particulate-based EPR oximetry is usually described as "minimally invasive" as only one-time implantation of the particulate spin probe is needed, and the subsequent measurements are carried out without any invasive procedure.

Despite all of these advantages, there exist numerous technical challenges that have limited the widespread use of in vivo EPR oximetry. Some of the technical problems encountered in EPR oximetry include nonresonant absorption at higher frequencies resulting in unwanted heating of aqueous samples, poor SNR, small penetration depth especially at higher frequencies, requirement of an exogenous probe, rapid bioreduction or excretion of soluble spin probes, long acquisition times, and motion artifacts.

3.1. Principle of EPR Spectroscopy

EPR was first discovered by Zavoisky in 1944. It is a branch of spectroscopy in which electrons with unpaired spins, when placed under a magnetic field, absorb electromagnetic radiation to transition from a low energy level to a high energy level. In principle, EPR is similar to NMR spectroscopy where the transition of protons between two energy levels is observed.

In EPR, the energy differences studied are primarily due to the interaction between the electronic magnetic moments and the external magnetic field, B_{ext}, also called the main magnetic field. Because of its magnetic moment, an unpaired election acts like a tiny bar magnet in the presence of an external magnetic field. It possesses the lowest energy if the magnetic moment is aligned with B_{ext} and the highest energy if it is aligned opposite to B_{ext} as shown in Figure 1. This is generally called the Zeeman effect.

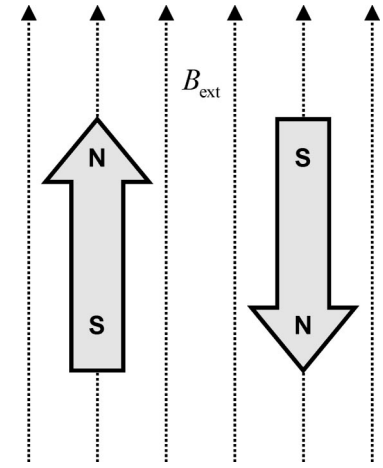

Figure 1. Lowest (left) and highest (right) energy orientations of the magnetic moment of an unpaired electron in the presence of an external magnetic field B_{ext}.

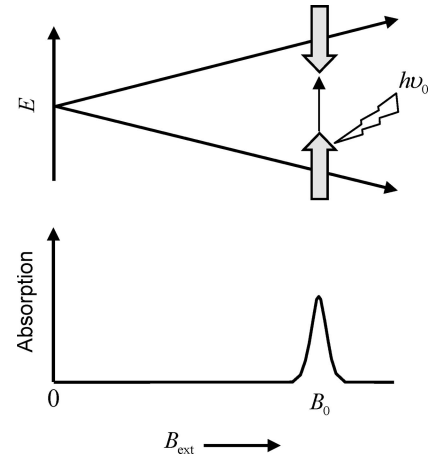

Figure 2. Zeeman splitting in the presence of an external magnetic field B_{ext} (neglecting second-order effects like hyperfine splitting).

Because an electron is a spin 1/2 particle, the low-energy and high-energy states can be designated as $M_s = -1/2$ and $M_s = +1/2$, respectively. The energy E of an unpaired electron in an external magnetic field B_{ext} can be defined as

$$E = g\beta M_s B_{ext} = \pm\frac{1}{2} g\beta B_{ext}$$
$$\Delta E = g\beta B_{ext} = \hbar\gamma B_{ext} \quad (1)$$

where ΔE is the energy difference between the two states, dimensionless g is the g-factor or g-value, β is the Bohr magneton, which is the unit of magnetic moment, $\gamma = g\beta/\hbar$ is the gyromagnetic ratio, and $\hbar$ is the reduced Plank's constant. If B_0 is the external magnetic field where ΔE in eq 1 matches the radiated energy $h\upsilon_0$, we can write

$$B_0 = \frac{2\pi\upsilon_0}{\gamma} = \frac{\omega_0}{\gamma} \quad (2)$$

where υ_0 is the frequency, in Hertz, of electromagnetic excitation, usually in the radiofrequency (RF) range.

The splitting between energy states, depicted in Figure 2, varies linearly with B_{ext} and is degenerate when $B_{ext} = 0$, which means that the two states have the same energy in the absence of an external magnetic field. In the presence of the external magnetic field, absorption of the electromagnetic radiation

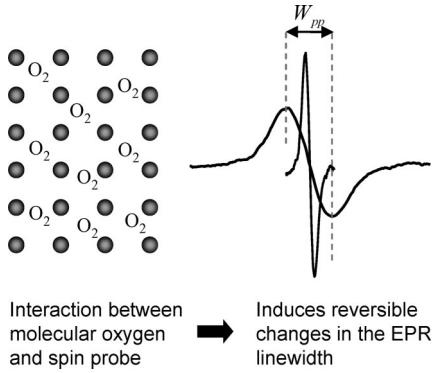

Figure 3. Effect of oxygen on exchange-narrowed line shape. Black dots represent spin probe molecules. Introduction of O_2 induces line broadening measured by peak-to-peak line width W_{pp}.

happens whenever eq 2 is satisfied. The condition can be satisfied either by fixing the radiation frequency and adjusting B_{ext} or by fixing B_{ext} and adjusting the radiation frequency. The limitation of RF hardware, however, makes the latter choice unattractive. At resonance, the unpaired electrons at the lower energy level absorb the RF radiation and jump to the higher energy state. These excited electrons move back to the lower energy state by releasing the excess energy. It is this transition between low and high energy states that is recorded in EPR.

Because the unpaired electron is exposed to its surrounding, nuclei with magnetic moments in the vicinity of an unpaired electron may affect the local magnetic field experienced by the unpaired electron, which may result in further splitting of the spectrum, called hyperfine splitting.[97] The presence of hyperfine structures in an EPR spectrum can provide a wealth of information regarding the free radical species and their environments.

3.2. Principle of EPR Oximetry

Molecular oxygen is a naturally occurring triplet radical and cannot be directly detected by EPR when in a dissolved state due to extremely short relaxation times.[98] Hence, the measurement of oxygen concentration by EPR (EPR oximetry) involves the use of an external spin probe consisting of paramagnetic material in either particulate (solid) or soluble form. The changes in the EPR line width of the exogenous spin probe are caused by the interaction of two paramagnetic species, molecular oxygen and the spin probe. The interaction includes a dipole−dipole interaction and Heisenberg spin exchange,[99] with the latter being the dominant interaction for the majority of commonly used soluble spin probes with low viscosities. The broadening of EPR spectrum, depicted in Figure 3, permits quantification of pO_2 or O_2 concentration.

The spin−spin relaxation rate, R_2, which is directly related to line width (W) and inversely related to relaxation time (T_2), increases with oxygen concentration. For soluble spin probes, the line broadening is caused by direct bimolecular collisions between two paramagnetic species, with the rate of collision, ω, given by the Smoluchowski equation

$$\omega = 4\pi r(D_P + D_O)C_O \quad (3)$$

where r is the interaction distance between the oxygen and the spin probe, D_P and D_O are the diffusion coefficients of the soluble spin probe and oxygen, respectively, and C_O is the oxygen concentration. Usually, D_O is much greater than D_P. Therefore, eq 3 can be approximated as

$$\omega = 4\pi r D_O C_O \quad (4)$$

Because the line width of the EPR absorption spectrum varies linearly with the collision frequency ω, the relationship between line width and oxygen concentration is expected to be linear. Therefore, the measured line width can be used to quantify oxygen concentration.

For particulate spin probes, line broadening is based predominantly on Heisenberg spin exchange.[90] In the absence of oxygen, the radicals of the particulate spin probe undergo intense Heisenberg electron−electron exchange, also called exchange narrowing, which results in a very narrow line shape. This phenomenon of exchange narrowing for paramagnetic resonance was first suggested by Gorter et al.[100] in 1947 and was later mathematically modeled by Anderson et al.[101] in 1953. In the presence of exchange narrowing, any line broadening, for instance, due to magnetic dipole interaction is narrowed by a fast dynamics resulting from the exchange coupling. With the introduction of oxygen, the spin exchange between two paramagnetic species—oxygen and the spin probe—results in reversible line broadening of the EPR spectrum.

The line broadening (ΔW) due to spin exchange between the spin probe and the O_2 can be written as[102]

$$\Delta W = AKC_O \quad (5)$$

where

$$K = p_A(4\pi d D_O) \quad (6)$$

and

$$A = \frac{2}{\sqrt{3}}\gamma_I \quad (7)$$

where d is the distance of closest approach of O_2 to a spin of the particulate probe, γ_I is the gyromagnetic ratio of the paramagnetic specie, C_O is the concentration of O_2 adsorbed into the probe, and p_A is the probability of spin exchange per collision, given by

$$p_A = \frac{4J^2T_1\tau_c}{3 + 4J^2T_1\tau_c} \quad (8)$$

Here, J is the exchange interaction between the spins of a colliding O_2 and the spins of particulate probe, τ_c is the mean interaction time, and T_1 is the oxygen relaxation time. For strong spin exchange ($p_A \approx 1$), eq 5 becomes

$$\Delta W \propto KC_O \propto D_O C_O \quad (9)$$

For many carbon-based particular spin probes, however, the dipole−dipole interaction, depending on the pore size of the material and the temperature, may become the leading contributor to the line broadening.[102]

On a pulsed EPR spectrometer,[103] the decay of magnetization, called free induction decay (FID), is recorded after applying an excitation pulse in the presence of a fixed magnetic field. On a continuous wave (CW) EPR spectrometer, the absorption spectrum is instead collected by subjecting the sample to a fixed monochromatic electromagnetic excitation and sweeping B_{ext}. The EPR spectrum, also referred to as the EPR line shape, is simply the Fourier transform of FID.[104] The most common line shapes are Lorentzian and Gaussian, but other nonparametric line shapes are not uncommon.

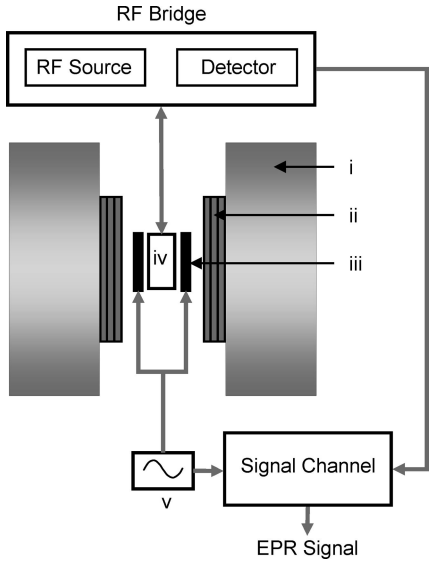

Figure 4. Basic layout of a CW EPR spectrometer and imager. Legend: i, main magnet; ii, gradient coil assembly; iii, field modulation coil; iv, resonator; and v, field modulation source.

3.3. Spectroscopy and Imaging

There are three modes of data collection in EPR—spectroscopy, spatial imaging, and spectral-spatial imaging. EPR oximetry can be performed in either the first (spectroscopy) or the third (spectral-spatial) mode. For spectroscopy mode, the EPR signal from the entire irradiated section of the sample is collected simultaneously. Because there are no magnetic gradients or other means of spatial encoding, no information is provided on the spatial distribution of spins. This method is quick and suitable for samples with spatially invariant line shapes. Spatial imaging does not provide any spectral information and is generally used to construct spin density maps. This mode is generally not used for oximetry, which is based on variations in the line shape. In spectral-spatial mode, both line shape and spin density are mapped by applying linear magnetic field gradients varying in both orientation and strength. Further details of data collection and processing for these three modes of EPR oximetry are discussed in section 5.

4. Instrumentation

Over the past few decades, many advances in EPR instrumentation have been made to improve SNR of the data and to reduce the data collection time. In this section, we discuss a basic layout of a CW EPR spectrometer and imager. The layout of a pulsed EPR system, which in principle is very similar to an MRI system, is discussed elsewhere.[105,106]

4.1. Basic Layout

A general layout of a CW EPR spectrometer and imager is shown in Figure 4. A static magnetic field is provided by a main magnet assembly. The gradient coils provide a linear magnetic field gradient necessary for spatial encoding in EPR imaging. The sample to be studied is placed in the cavity, also called the resonator, which helps to amplify weak EPR signals. The detector and electromagnetic radiation sources are housed in a box called the RF bridge. The signal channel primarily consists of a phase-sensitive detector.

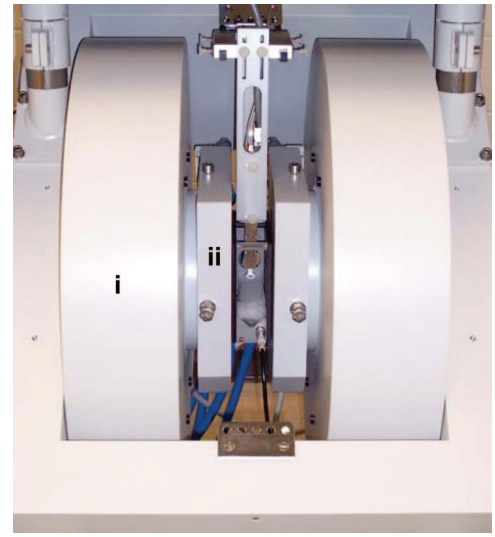

Figure 5. Bruker (Bruker BioSpin, Billerica, MA) L-band EPR imager. Main magnet (i) and magnetic field gradient assembly (ii).

4.1.1. Main Magnetic Field

The design of the magnetic field system for EPR spectroscopy and imaging defines the size and geometry of samples that can be studied. The requirements of field homogeneity are more stringent for larger samples and for narrower line shapes. In general, the system must provide a magnetic field with across volume inhomogeneity smaller by an order of magnitude than the smallest line width being measured.

Generally, three types of magnets are utilized in the existing EPR imaging designs, namely, nonferrous electromagnets,[107] iron core electromagnets,[108] and permanent magnets.[109] For low-field systems with static fields up to 500 Gauss, nonferrous electromagnets can be used. These magnets may utilize Helmholtz coil design, solenoidal design, or some type of hybrid multicoil design for improved homogeneity of the field. These electromagnets provide the advantage of simple current control of the field due to the absence of hysteresis effects associated with the iron core. However, low energy efficiency of such magnets limits the achievable field strength to several hundred Gauss.

Historically, the iron core electromagnets used in EPR spectrometers found the most widespread use in higher field EPR systems (RF to X-band). Typically, such a system utilizes a large pole-face electromagnet (15″ and over) with custom-machined pole pieces to further increase the gap.[110] Permanent magnet-based systems have not gained a wide use due to poor thermal stability of the field and, thus, a need for elaborate systems of compensation coils and electronics. To ensure the stability of the magnetic field, for any magnet type, the Hall effect sensor-based feedback is generally used. Figure 5 shows the main magnet and magnetic field gradient assembly for an L-band EPR imager.

4.1.2. Gradient Coils

EPR imaging imposes extremely stringent requirements for magnetic field gradient design when compared to MRI. This is due to the fact that strong linear gradients (more than an order of magnitude stronger than for clinical MRI systems, which are typically in the range of 1−4 G/cm) are required to obtain high spatial and spectral resolution due to the much

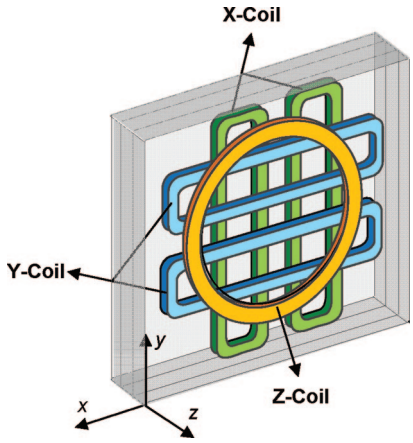

Figure 6. Gradient coil assembly. The left-side enclosure of a 3D gradient coil assembly is shown. The *Z*-gradient is generated using Maxwell coils, while *X*- and *Y*-gradients are generated using flat pair coils.

broader line shapes of EPR spectra. Also, in CW EPR imaging, the gradients must be able to dissipate peak power during long periods of time. Transient response, however, is less important than that for MRI so that active shielding is usually not necessary. As the sample size increases, problems imposed by the need for powerful field gradients escalate since the power required to generate a given gradient increases with the cube of the gap distance between the coils of the main magnet. Dissipation of the power in the coils also becomes more difficult as the surface/volume ratio of the coil decreases.

Two distinct gradient coil designs are selected for the two major geometries of main magnetic field coil designs, which are Helmholtz pair coils and a solenoidal coil.[111] The *Z*-gradient coils, for either of the main magnetic field coil designs, are in a Maxwell pair coil configuration. However, for *X*- and *Y*-gradient coils, the use of flat square pairs (four coils per axis as shown in Figure 6) is preferred for the Helmholtz main field geometry, while a curved Golay gradient coil design[112] is required for the solenoid electromagnet to conform with the cylindrical geometry. A system of multiple computer-controlled power supplies must be utilized to drive the gradient coils as required by the projection acquisition sequence. Ideally, these power supplies are a bank of switching mode operational power amplifiers capable of four-quadrant operation with an IEEE-488 or other computer interface.

4.1.3. RF Bridge

The RF bridge handles the generation of RF signal and the detection of the EPR signal coming out of the resonator. Key components of a typical RF EPR bridge, labeled in Figure 7, are briefly described below.

i. Oscillator: It is used to generate RF energy. The frequency of RF energy is generally varied with mechanical and electrical means. While mechanical adjustments are used for coarse tuning, electronic adjustments are applied for fine tuning. The oscillator must have a stable output frequency and amplitude, as even slight changes can introduce distortion in the data.

ii. Attenuator: It precisely controls the amount of RF energy delivered to the resonator. It must be very stable over time and a broad temperature range.

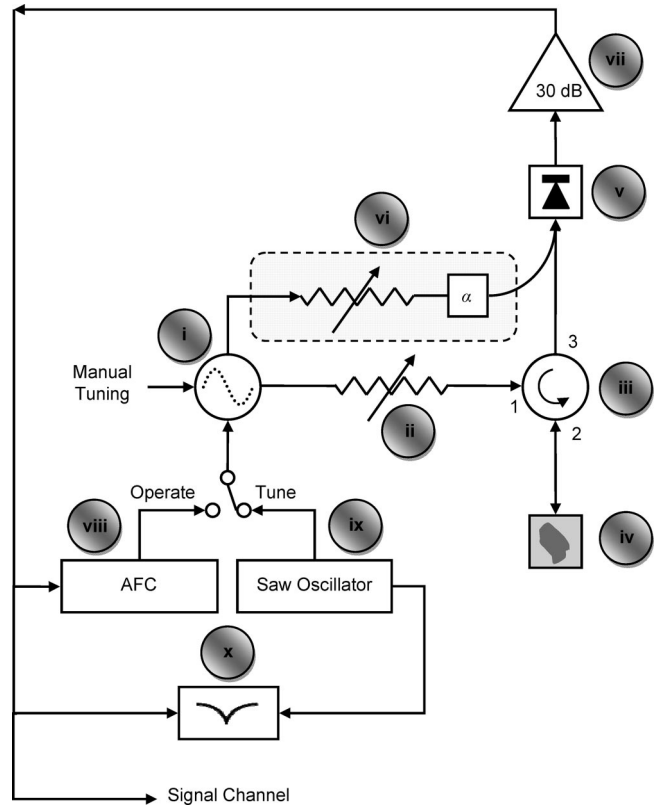

Figure 7. Layout of a typical CW EPR bridge. Adapted with permission from Eric Kesselring.

iii. Circulator: The circulator allows reflected energy from the resonator at port 2 to reach the detector diode at port 3 while blocking high-level excitation energy from port 1 to reach port 3.

iv. Resonator: The resonator is used to amplify small changes induced in the RF radiation due to the magnetic resonance of the sample. The change in RF energy absorbed by the sample, upon magnetic resonance, changes the impedance of the resonator. This change in impedance changes the reflection coefficient of the resonator, resulting in reflected RF power fluctuation. In CW EPR, it is this fluctuation of the reflected RF power that is converted into an EPR signal.

v. Detector: It converts RF energy reflected from the resonator into a baseband signal. It is generally comprised of a diode detector and a passive low pass filter. The electrical output signal from a typical detector diode is 1500 mV output per mW of RF input. Because excessive RF power can permanently damage the diode, additional protection circuitry is included to monitor and limit the diode current

vi. Reference arm: It is used to apply small RF power to bias the detector diode into the more sensitive operating region. An RF phase (α) shifter synchronizes reference arm power with the reflected power from the resonator. Many home-built units do not have a reference arm and require off-resonance coupling of the resonator for the bias.

vii. Preamplifier: It amplifies the small signal (typically less than 10 mV) from the detector for further filtering and amplification by lock-in detector (signal channel).

viii. AFC: The automatic frequency controller modulates the frequency of the RF source with a 70 kHz signal. It further processes the 70 kHz component of the signal coming from the preamplifier to provide feedback to electronically match the RF oscillator frequency to that of the resonator.
ix. SAW oscillator: It generates sawtooth waveform (in the range of 400 Hz) to provide a frequency sweep for the tuning mode.
x. Tuning display: It displays an oscillator frequency sweep (x-axis) versus reflected power from the resonator (y-axis) during the tuning mode. It allows visual feedback for tuning the oscillator frequency to the resonator frequency.

4.1.4. Resonator

The EPR resonator design is important to maximize sensitivity and must be tailored to accommodate the sample with the highest possible filling factor × quality factor product. The quality factor, Q, is the ratio of energy stored to energy lost by the resonator, while the filling factor is the fraction of total RF magnetic field power entering the resonator that is incident upon the sample. A higher Q allows larger detectable changes during absorption and hence improves signal intensity.

The resonator must be a mechanically stable structure and should make most efficient use of the space within the magnet. Space constraints present a major consideration in the choice of the resonator design for EPR imaging. Innovations in resonator design, which enable automatic coupling adjustment and frequency tuning,[113,114] can be used to suppress motion-induced distortion that occurs in biological samples.

In recent years, much effort has been focused on the development of lumped-parameter RF sample cavities for L- and S-bands. Two major types of such resonators, namely, loop-gap and reentrant, have been introduced and extensively discussed in the literature.[115,116]

Loop-gap resonators (LGRs) provide a straightforward design and high filling factors as compared to standard distributed parameter RF cavities. However, because of the open structure of the inductive loop element, LGRs have significant radiation losses unless a shield is provided. The need for the shield leads to problems in achieving an optimum magnitude of modulation field and at least a 20% increase of overall resonator dimensions. A sketch of a loop-gap surface resonator design, originally developed by Bacic et al.,[117] is shown in Figure 8a. The reentrant resonator (RER) design was introduced and described in great detail by Sotgiu.[116] Because the resonant structure of the RER forms a closed volume, it does not require any additional shield, thus providing substantial space savings as compared to LGRs. A number of RERs constructed of ceramic silver-plated material are also reported,[118] offering improved rigidity and stability. Figure 8b shows an RER resonator design for a L-band EPR.

4.1.5. Modulation Coil and Signal Channel

To improve the system sensitivity, it is a common practice in CW EPR to modulate B_{ext} by adding an oscillating magnetic field using a pair of modulation coils and to detect the signal using a phase-locked loop detector, which is also called a phase-sensitive or a lock-in detector. The lock-in detector compares the EPR signal from the crystal with the reference signal, which comes from the same oscillator that generates the magnetic field. The lock-in detector only accepts the EPR signal that is phase coherent to the reference signal.[119] The advantages of lock-in detection include less $1/f$ noise from the detection diode and elimination of the baseline instabilities due to drift in DC electronics. It is important to note that for certain data collection methods, rapid scan[120] for instance, no field modulation is applied and the absorption signal is recorded directly.

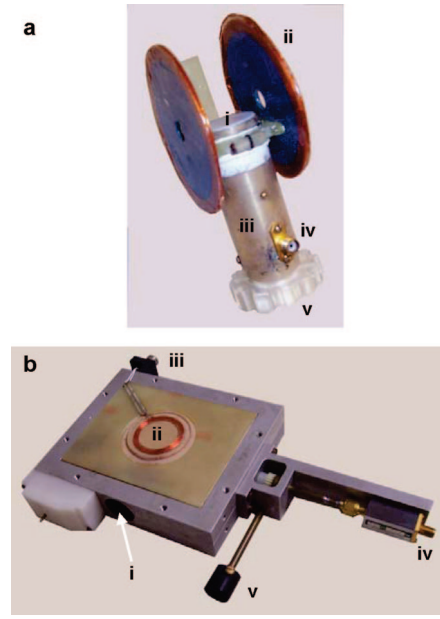

Figure 8. Two frequently used resonator designs for EPR spectrometer. (a) Surface-bridged, loop−gap resonator (LGR). The LGR structure is housed inside a metallic tubular shield. Legend: i, active surface area for sample; ii, field modulation coils; iii, resonator shield; iv, RF input connector; and v, coupling adjustment ring. The connector for the field modulation coil is not visible from this view. The resonant frequency of this unloaded LGR was 1.25 GHz. (b) Volume RER. The RER houses a cylindrical cavity of 24 mm diameter and 22 mm of effective length. Legend: i, sample cavity opening; ii, modulation coils; iii, connector of modulation coils; iv, RF input connector; and v, coupling adjustment knob. The resonant frequency of this unloaded RER was 1.27 GHz.

4.2. Tuning Parameters

There is an array of instrument parameters, which, when adjusted properly, can improve the performance of the spectrometer or imager for a given oximetry application. Selection of these parameters depends on the experimental setup, such as sample size, and the nature and extent of information sought.

Here, we briefly mention some of the important instrument setup parameters that affect the SNR and hence the acquisition time and the accuracy of final results. (i) Radiation frequency: An increase in the radiation frequency improves the SNR but at the same time results in unwanted nonresonant absorption and reduction in penetration depth. (ii) Magnetic gradient: An increase in magnetic gradient strength thermally burdens the gradient coils and degrades SNR but improves spatial resolution. (iii) RF power: An increase in RF power improves SNR but may also result in heating of the sample and power saturation-induced line broadening. (iv) Quality factor: A high Q of a resonator, along with critical coupling, improves SNR but also leads to extra

sensitivity to sample motion. (v) Modulation amplitude: An increase in modulation amplitude improves SNR but exerts extra burden on the modulation coils and also results in line shape distortion, which is generally corrected by postprocessing.[121] (vi) Sweep time: Increasing the magnetic field sweep time for each spectral scan improves SNR but prolongs the acquisition time, which can be very critical for in vivo applications. (vii) Number of projections: For imaging, collecting data along a large number of orientations generally improves reconstruction quality but only at the cost of increased acquisition time.

5. Data Collection and Processing

5.1. Spectroscopy

In spectroscopy, the measurements take place in the absence of a magnetic field gradient. Hence, no information is captured regarding the spatial distribution of the spin probe. The collected information is solely limited to the shape of the composite spectrum. If there is more than one paramagnetic species present in the sample, the observed signal is the superposition of individual spectra.

5.1.1. Data Collection

Although in principle it is possible to sweep the RF frequency for a fixed B_{ext}, the related hardware challenges make it an unattractive option. Therefore, in CW EPR, the spectrum is generally observed, in the presence of a fixed frequency excitation, by sweeping B_{ext}

$$B_{ext} = B_0 + B_\delta \tag{10}$$

where B_δ represents field sweep and B_0, defined by eq 2, is the magnetic field strength at which magnetic resonance occurs. For a majority of spin probes, the line shape l belongs to family of parametric functions such as Lorentzian, Gaussian, or Voigt.[122] A Lorentzian line shape with full-width at half-maximum (FWHM) line width W and amplitude, κ, which is the area under the absorption curve, is defined in eq 11

$$l(W,\kappa) = \frac{\kappa}{\pi}\frac{0.5W}{(B_\delta)^2 + (0.5W)^2} \tag{11}$$

As mentioned earlier, SNR can be improved by modulating the magnetic field and observing the first harmonic, which, for small modulation amplitude B_m, represents the first derivative[123] of l as shown in Figure 9.

5.1.2. Data Processing

For oximetry, line width for an oxygen sensitive spin probe increases monotonically with the pO_2 to which the spin probe is exposed. Hence, measuring W can provide a direct reading of pO_2. For spectroscopy, the data processing involves estimating line width from noisy measurements. For high SNR, a direct peak-to-peak measurement can be used to estimate line width. For low SNR, however, curve fitting, shown in Figure 10, can be applied to improve robustness. For curve fitting, the measured noisy spectrum is fitted to a known parametric line shape of the spin probe.

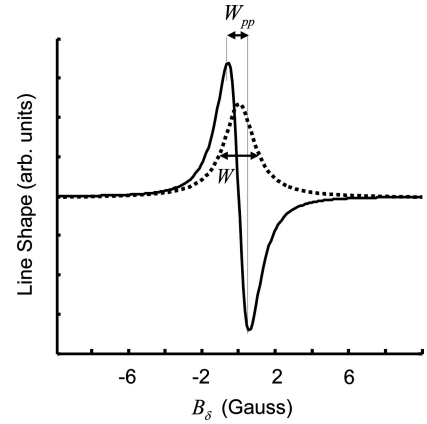

Figure 9. Lorentzian line shape (dotted line) with FWHM line width $W = 1$ G. First derivative Lorentzian line shape (solid line) with peak-to-peak line width $W_{pp} = 0.58$ G. For a Lorentzian line shape, $W_{pp} = W/\sqrt{3}$.

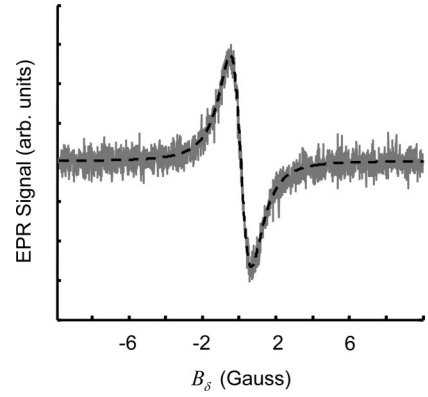

Figure 10. Measured data (gray line) are generally noisy, and curve fitting (dashed line) is applied to extract the line width information.

5.2. Spatial Imaging

Spatial EPR imaging is capable of providing the distribution of paramagnetic spins in the 1D, 2D, or 3D spatial domain[124,125] $\boldsymbol{u} \in \mathbb{R}^d$. Application of a magnetic field gradient $\boldsymbol{g}_u$ is used to resolve the spatial distribution of spin probes. In spatial imaging, it is assumed that the line shape of the spin probe is spatially invariant. In cases where line shape changes with the location (possibly due to changes in the environment such as variations in pO_2) or where there are multiple spin probes with different line shapes, it may not be possible to provide an accurate distribution of the spin probes using purely spatial EPR imaging. Although spatial imaging is not used for oximetry, a basic understanding would help the reader comprehend the concept of spectral-spatial imaging, which is discussed later.

5.2.1. Data Collection

The net external magnetic field in the presence of a gradient $\boldsymbol{g}_u$ becomes

$$\begin{aligned} B_{ext} &= B_0 + B_\delta + \langle \boldsymbol{g}_u, \boldsymbol{u} \rangle \\ B_{ext} - B_0 &= B_\delta + \langle \boldsymbol{g}_u, \boldsymbol{u} \rangle \end{aligned} \tag{12}$$

where $\langle ., . \rangle$ represents the inner product. The resonance condition is only met where $B_\delta + \langle \boldsymbol{g}_u, \boldsymbol{u} \rangle = 0$. Each term in eq 12 has units of magnetic field but can be converted to spatial units by dividing both sides by $-|\boldsymbol{g}_u|$.

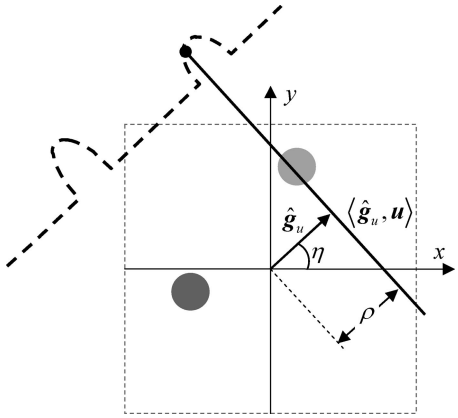

Figure 11. Projection acquisition for a 2D spatial digital object. Angle η defines the orientation of the applied gradient g_u, and ρ defines the distance of resonant plane $\langle \hat{g}_u, u \rangle$ from the origin.

For EPR imaging, data are collected in the form of projections. A projection p is computed by the Radon transform (RT) of a 2D or 3D object f

$$p(\rho, \hat{g}_u) = \int_u f(u)\, \delta(\rho - \langle \hat{g}_u, u \rangle)\, du \qquad (13)$$

where $\rho = -B_\delta/|g_u|$ and $\hat{g}_u = g_u/|g_u|$. Here, $\langle \hat{g}_u, u \rangle$ is the plane to be integrated, and ρ is the distance of this plane from the center of image space as shown in Figure 11. For a spin probe with line shape $l_\rho(W_\rho, \kappa)$, each measured projection is a convolution of a true projection obtained by RT and the line shape $l_\rho(W_\rho, \kappa)$.

$$p_l(\rho, \hat{g}_u) = p(\rho, \hat{g}_u) \otimes l_\rho(W_\rho, 1) \qquad (14)$$

where $\otimes$ stands for convolution in the first variable. Note that $l_\rho(W_\rho, \kappa)$ is the line shape in spatial domain and $l(W, \kappa)$ is the line shape in terms of magnetic field and is related to the former by

$$l(W, \kappa) = \frac{1}{|\hat{g}_u|} l_\rho(W_\rho, \kappa) \qquad (15)$$

where $W = |g_u| W_\rho$.

5.2.2. Data Processing

For EPR spatial imaging, data processing involves reconstructing 2D or 3D images from a set of collected projections. It is a linear inverse problem and has been discussed extensively.[126] Generally, filtered backprojection (FBP) or direct Fourier method is used to reconstruct the image. For a small number of projections, the reconstruction using FBP may result in undesired streak artifacts. To overcome this problem, iterative reconstruction methods[127,128] can be used to improve the reconstruction quality at the cost of reconstruction time. The effect of spatial blurring, represented in eq 14, can be suppressed by applying higher gradient $|g_u|$. For situations where the application of a large enough gradient is not possible due to SNR degradation or hardware limitations, deconvolution[129] is applied either before or during the reconstruction. A common practice is to perform deconvolution on individual projections before the reconstruction. The most common method of performing deconvolution is by a point-by-point division, in the discrete Fourier domain, of each measured 1D projection by the measured or calculated line shape. To avoid a divide-by-zero problem, each projection is lowpass filtered before the deconvolution.

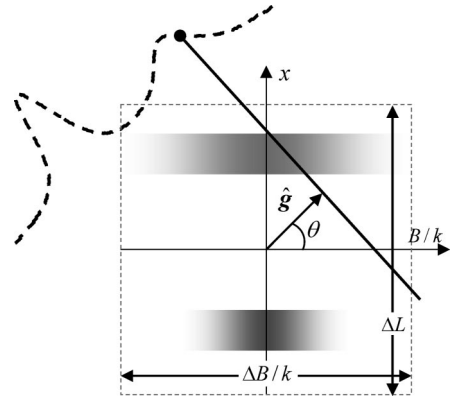

Figure 12. Data collection for a 2D spectral-spatial digital object. The vertical axis represents the spatial dimension, while the horizontal axis represents the spectral dimension. The figure shows two regions; the one on the top has a large line width, while the one on the bottom exhibits a smaller line width. Here, $k = \Delta B/\Delta L$, and $\hat{g} = (\hat{g}_u \sin \theta, \cos \theta)$ is a generalized gradient vector that incorporates gradient strength with gradient orientation.

5.3. Spectral-Spatial Imaging

For samples having variable line widths, which is the case for EPR oximetry, it is not possible to obtain an accurate map of the spin distribution using data collection and image reconstruction procedures used for purely spatial EPR. Furthermore, the information obtained by purely spatial EPR imaging is limited to the spin density and cannot resolve the nature of the spins at each spatial volume element (voxel). To overcome this limitation, an additional spectral dimension is considered to capture the line shape at each voxel. The imaging technique that includes a spectral dimension along with one or more spatial dimensions is termed as spectral-spatial imaging.[130]

5.3.1. Data Collection

For spectral-spatial imaging, the spatial information is captured by collecting projections along different spatial orientations of the gradient vector, while the spectral information is captured by varying the gradient strength in addition to the orientation. Spectral-spatial imaging can be performed in 1, 2, or 3 spatial dimensions giving rise to 2D, 3D, or 4D spectral-spatial images, respectively. Conceptually, the data acquisition in n spatial and one spectral dimension is similar to the data acquisition in $n + 1$ spatial dimensions. To augment the spectral dimension, an addition angle, θ, also called a spectral angle, is introduced. The spectral angle is defined as

$$\tan \theta = \pm \frac{|g_u| \Delta L}{\Delta B} \qquad (16)$$

where ΔL and ΔB define the size of the field-of-view along spatial and spectral dimensions, respectively. Figure 12 shows the data collection scheme for a 2D spectral-spatial object.

5.3.1. Data Processing

Conceptually, image reconstruction for spectral-spatial imaging is identical to spatial imaging with the exception

of an added dimension. Generally, after rescaling of the collected projections to accommodate for the signal loss at higher gradient strengths, FBP is applied to obtain a spectral-spatial image. For high gradient projections, time averaging is applied to partially compensate for the SNR loss. Also, because of limited gradient strength, it is not possible to collect projections with the spectral angle values in the vicinity of $\pm\pi/2$, which leads to the problem of image recovery from an incomplete data set. This is usually referred to as limited-angle tomography and has been studied extensively.[131] Spectral-spatial imaging is generally time-consuming, especially in 4D where hundreds or even thousands of projections are collected, with each requiring a sweep time of a couple of seconds or more.

5.4. Recent Developments

EPR oximetry, especially when performed over three spatial dimensions, is time-consuming, which has adversely affected the wide use of EPR for clinical applications. Several innovations, ranging from improved hardware designs to optimized data collection and processing schemes, have been implemented to reduce the data collection time to the levels suitable for in vivo studies. However, there is still room for further acceleration of data acquisition before EPR can be declared a serious contender for clinical oximetry. In this section, we look at some of the data collection and processing methodologies adopted by the EPR community to speed up data acquisition.

5.4.1. Pulsed System

In CW EPR, the data are collected by exposing the sampling to a fixed frequency excitation and sweeping the magnetic field gradually. It may take a couple of seconds or more to acquire one projection. Therefore, acquiring data for higher dimensions, where hundreds and even thousands of projections may be required, becomes impractical for many applications where conditions may change rapidly. Pulsed EPR, on the other hand, has the potential to reduce the acquisition time substantially.[106] However, there are numerous technical challenges still to be addressed before pulsed EPR overtakes CW EPR for broad EPR applications. In pulsed EPR, the excitation is provided by a train of short RF pulses, and the emitted signal from the spins, called FID, is digitized and recorded. The EPR spectrum can be obtained by simply applying the Fourier transform to the FID. Although the basic principle of the pulsed EPR spectrometer is similar to that of NMR, extremely short relaxation times for EPR make the instrumentation much more challenging. At low frequencies, the dead time of an EPR resonator, defined as the time required by the resonator to dissipate the RF energy, can approach the relaxation times of many commonly used spin probes, making it extremely difficult to collect the data. Therefore, spin probes with longer relaxation times are highly preferred to exploit the advantages of the pulsed system. Lately, there has been a renewed interest in the development of a low frequency pulsed EPR system.[132]

5.4.2. Overmodulation

Modulation amplitude is another important parameter that affects the data quality. In the presence of a modulating field $B_m \cos \omega_m t$ and without the application of the gradient, eq 12 can be written as

$$B_{ext} - B_0 = B_\delta + B_m \cos \omega_m t \tag{17}$$

where B_m is the modulation amplitude. Equation 11 then becomes

$$\begin{aligned} l(W, \kappa, B_m) &= \frac{\kappa}{\pi} \frac{0.5W}{(B_\delta + B_m \cos \omega_m t)^2 + (0.5W)^2} \\ &= \frac{\kappa_0}{(2/W)^2 (B_\delta + B_m \cos \omega_m t)^2 + 1} \end{aligned} \tag{18}$$

where $\kappa_0 = 2\kappa/\pi W$ is the amplitude of l at $B_\delta = 0$. In terms of a Fourier series

$$l(W, \kappa, B_m) = \kappa_0 \left[a_0 + \sum_{n=1}^{\infty} a_n(W, B_\delta, B_m) \cos n\omega_m t \right] \tag{19}$$

where

$$a_n = \frac{\omega_m}{\pi} \int_{-\pi/\omega_m}^{\pi/\omega_m} \frac{0.5W \cos n\omega_m t}{(B_\delta + B_m \cos \omega_m t)^2 + (0.5W)^2} \tag{20}$$

The closed form expression for a_n can be calculated by contour integration. To observe the first harmonic, a_1, the signal at the output of the lock-in detector is multiplied with $\cos \omega_m t$ and lowpass filtered. For B_m that is much smaller than W, the first harmonic is approximately equivalent to the first derivative of the absorption signal. When B_m increases so does the signal intensity, but the signal gets distorted and no longer remains Lorentzian as shown in Figure 13. Fortunately, this modulation induced distortion is well-characterized.[121] To improve the SNR, the use of B_m that is much larger than W has been reported.[133,134]

5.4.3. Rapid Scan

In traditional CW EPR, a slow linear scan is made to collect a spectrum or a projection. The magnetic field modulation and the lock-in detection are applied to increase SNR. In rapid scan, the magnetic field is swept back and forth at a high rate, usually in the kHz range, and the absorption signal is recorded directly without any field

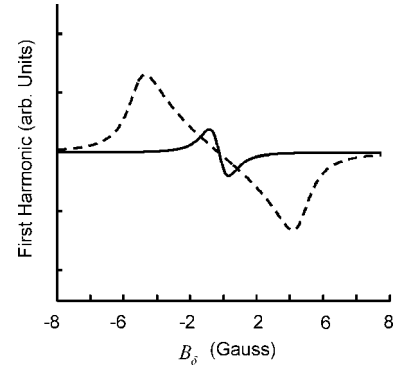

Figure 13. Effect of modulation amplitude B_m on line shape. The solid line represents the line shape for a modulation amplitude that is 10% of line width W, while the dashed line represents the line shape for a modulation amplitude that is 250% of W.

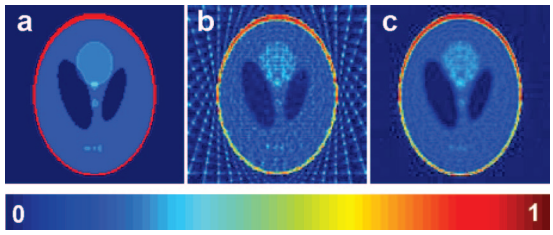

Figure 14. Comparison of an iterative reconstruction method with the commonly used FBP method. (a) A 128 × 128 2D digital Shepp−Logan phantom. (b) Reconstruction from FBP using 20 noiseless projections; after the reconstruction, all pixels with negatives values were set to zero. (c) Reconstruction based on ART with nonnegativity constraint using 20 noiseless projections.

modulation or lock-in detection. For scan rates comparable to the relaxation times, a distortion is introduced in the spectrum. Fortunately, this distortion is well-characterized using Bloch equations and can be easily accounted for by postprocessing.[135] When the RF power is optimized for a given scan rate, the signal intensity is enhanced by up to a factor of 3 relative to the conventional slow scan lock-in detection.[120] Also, the SNR for rapid scan is inversely proportional to the magnetic field sweep width as compared to the lock-in detection where the SNR is inversely proportional to the square of the magnetic field sweep width. The relative performance of rapid scan has been evaluated for EPR recently.[136] High scan rates, usually in the kHz range, make rapid scan the method of choice for EPR imaging of a moving object such as beating heart.

5.4.4. Iterative Reconstruction

Iterative methods, also known as series expansion reconstruction methods or algebraic reconstruction methods, have been used for tomographic reconstruction for the last few decades.[127] These methods are based on the discretization of the image domain prior to any mathematical analysis, which is in contrast to the transform methods, such as the FBP, where the continuous problem is only discretized as the last step of the reconstruction process.[137]

Iterative methods are computationally intensive, but the reconstruction is usually superior to the FBP. Algebraic reconstruction technique[138] (ART) is a common iterative method used to reconstruct data from projections. The most attractive feature of ART, and other similar iterative techniques, is its ability to merge a variety of constraints into the iterative process. For example, a nonnegativity constraint can be readily implemented by setting the negative portions of the estimate to zero in each iteration. Furthermore, the iterative methods do not require projections to be uniformly distributed; hence, the missing angle problem is handled seamlessly. A comparison of ART reconstruction and FBP reconstruction from 20 noiseless projections for a 2D digital Shepp−Logan phantom is represented in Figure 14. A strong streak artifact is visible for the FBP reconstruction.

For spatial imaging, another major advantage of iterative methods is their ability to incorporate the deconvolution step into the interactive scheme, eliminating the need for a separate deconvolution that generally yields poor results. Computationally efficient algorithms have been reported to carry out the iterative reconstructions from projection data.[139] Recently, a number of iterative methods have been suggested for EPR image reconstruction, each differing in the cost function to be minimized.[140,141]

5.4.5. Single-Point Imaging (SPI)

SPI or constant-time imaging[142] is a special way of collecting data using pulsed EPR. In SPI, for every pulsed RF excitation, a single data point of the FID after a fixed delay in the presence of static magnetic field gradients is acquired. It is analogous to performing pure phase encodings in all dimensions to fill the *n*D Fourier domain point by point. Because the phase-encoding time (the fixed delay after excitation) remains constant for a given image data set, the spectral information (line shape) is automatically deconvolved, providing well-resolved pure spatial images. Therefore, SPI has the potential to provide high-resolution artifact-free images, which can be useful for many biological applications. For spectral-spatial imaging, the spectral information can also be extracted from a series of SPI images each corresponding to a different delay from the excitation pulse. Because only one data point is recorded per excitation, acquisition times for SPI can be longer than that for CW EPR imaging.

5.4.6. Spinning Gradient

Conventionally, the main magnetic field is slowly swept for a given gradient orientation, and the process is repeated for a set of different gradient orientations. For such an acquisition, the adjacent data points in each projection are highly correlated, resulting in data redundancy. For a spinning gradient, on the other hand, the main magnetic field is kept fixed, while the gradient orientation is rotated rapidly, and the process is repeated for different values of the main magnetic field. The resulting data have lesser redundancy and generate better quality images. The performance of spinning gradient-based data acquisition has been explored for EPR by Deng et al.[143] Usually, special low-inductance gradient coils are used to spin the gradients rapidly. If the spinning frequency is low (<100 Hz), the existing systems with phase-sensitive detection can be used without any major hardware modifications.

5.4.7. Multisite Oximetry

Swartz et al.[144] have pioneered an approach coined "multisite oximetry". A single favorable gradient direction is assumed for which each of several isolated implants is resolved. The EPR line shape for the spin probe material is assumed to be Lorentzian, with unknown line widths. A spectrum is recorded for two gradient magnitudes. The line widths are then estimated by nonlinear least-squares curve fit; the curve fit is computed on intervals for which spectral components are nonoverlapping. In this manner, the line width of each spin probe site is estimated without reconstruction of the entire spectral-spatial object. The key assumption is that line shapes are resolved with a single, 1D magnetic field gradient. The approach has been applied for in vivo oximetry of transient focal cerebral ischemia in the rat.[134] Recently, Som et al.[145] proposed a model-based approach to solve the multisite problem with much more favorable constraints on the experimental setup. For four isolated implants of a particulate spin probe, acquisition time reduction of 40:1 was reported in this study.

5.4.1. Digital Detection

Digital detection,[146] for both pulsed and CW EPR, has been gaining interest lately. There are several classes of digital detectors proposed for EPR,[147] including homodyne detection

followed by A/D conversion, superheterodyne detection followed by A/D conversion, time-locked subsampling (TLSS) of intermediate frequency carrier, and TLSS of RF carrier. In TLSS of intermediate frequency carrier, RF signal is first bandpass filtered and downconverted to intermediate frequency and then subsampled in a time-locked manner. For CW with field modulation, the main advantage of digital detection is the ability to simultaneously collect data across multiple harmonics of both absorption and dispersion signals. With the quality of digital hardware improving rapidly, digital detection will gain further popularity in the years to come.

5.4.1. Overhauser Enhanced MRI (OMRI)

OMRI combines the advantages of MRI with the sensitivity of EPR. It is a double resonance technique[148] that is based on the Overhauser effect.[149] In the presence of an exogenous, soluble spin probe, MRI measurements are recorded both with and without RF irradiation. The map of the difference between the intensities of two MRI reconstructions is related to the line width map of the spin probe. OMRI has been applied to study oxygenation of murine tumors.[150] Despite all of the advantages, high RF power and long RF irradiation times are required to obtain good signal enhancement in OMRI.[151]

6. EPR Oximetry Spin Probes

In living systems, free radicals and other paramagnetic species are either present at a very low concentration or have very short relaxation times, prohibiting their direct measurement. For instance, the relaxation time (T_1) for molecular oxygen dissolved in several solvents was found to be approximately 7.5 ps,[98] making the direct measurement using current EPR spectrometers impossible. Therefore, in all EPR oximetry applications, an exogenous material, called a spin probe or spin label, is delivered into the biological system, and the interaction of endogenous paramagnetic species, molecular oxygen in the case of oximetry, with the spin probe is used to quantify the endogenous specie.

6.1. Development

For the past two decades, several spin probes for EPR oximetry have been developed and extensively analyzed for biological applications. There are two classes of spin probes, namely, soluble and particulate spin probes. An appropriate choice of spin probe depends upon the experimental setup and the nature of desired information. Some of the pertinent properties of a spin probe include the following:

(i) Spin density: A higher spin density leads to higher SNR and ensures administration of smaller quantities of spin probe and shorter acquisition times.
(ii) Sharp line shape: A single sharp line shape improves SNR and reduces data acquisition times.
(iii) Power saturation: RF power saturation broadens the line shape and degrades SNR. A high threshold for power saturation allows for stronger RF irradiation without the saturation-induced broadening.
(iv) Oxygen sensitivity: It is defined as the change in line width for unit change in pO_2. Generally, a higher oxygen sensitivity is desirable for accurate pO_2 measurements, but excessive broadening of line shape due to high oxygen sensitivity may lower the SNR.

Table 1. Anoxic Line Width and Oxygen Sensitivity Values for Some Commonly Used EPR Oximetry Spin Probes[a]

spin probe	spin density (spins/g) × 10^{19}	anoxic peak-to-peak line width (mG)	oxygen sensitivity (mG/mm Hg)
LiPc	10	10−14	6.1−9.5
LiPc-α-OPh		530	13.7
LiNc	68	510	30
LiNc-BuO	72	210	8.5
Fusinite	1−2	800	25
Gloxy	4.6	550	27
India Ink	2.5	650	420
Tempone		330	0.64
TAM		90	0.84

[a] Values for LiPc were from Liu et al.[156] and Ilangovan et al.;[157] values for LiPc-α-OPh were from Pandian et al.;[158] values for LiNc were from Manivannan et al.;[159] values for LiNc-BuO were from Pandian et al.;[160] values for Fusinite were from Vahidi et al.[161] and Smirnova et al.;[162] values for Gloxy were from James et al.;[163] values for India Ink were from Goda et al.;[164] values for Tempone were from Shen et al.;[165] and values for TAM were from Dhimitruka et al.[166]

(v) Biostability: Biostability of a spin probe ensures that it does not degrade or lose it properties in a biological environment.
(vi) Chemical toxicity: It measures the extent of damaging effect, besides the injury caused by the implantation, which a spin probe may have on biological system.
(vii) Distribution: It refers to spatial distribution of the spin probe in the sample. Soluble spin probes tend to distribute more evenly, while particulate spin probes tend to stay localized. Table 1 summarizes anoxic line widths and oxygen sensitivities for commonly used oximetry spin probes.

6.1.1. Soluble Spin Probes

For oximetry, the main advantages of soluble spin probes include even distribution in the sample, access to deep organs, and automatic removal (by bioreduction or excretion) from the in vivo system. Nitroxides were among the first spin probes used for EPR oximetry.[152] Use of both five- and six-membered nitroxides has been extensively reported for a wide array of EPR oximetry applications.[153−155] Some of the commonly used nitroxides are shown in Figure 15a,b.

Nitroxide synthesized with ^{14}N has an EPR spectrum with three lines, while the nitroxide synthesized with ^{15}N exhibits an EPR spectrum with two lines. As compared to particulate spin probes, the EPR signals from nitroxides exhibit low SNR and poor sensitivity to oxygen. A number of improvements, including use of perdeuterated nitroxides[167] and encapsulation of nitroxides in lipophilic environments,[168] have been suggested to improve oxygen sensitivity. The synthesis of nitroxides can be manipulated to affect their bindings and hence distribution in a biological sample. For instance, a charged nitroxide cannot permeate the cellular membrane, while a neutral nitroxide can, giving a spin probe distribution in both intracellular and extracellular compartments.[169] Howard Halpern, over the last 25 years, has contributed immensely to the development of nitroxides for EPR measurements.[170,171]

Nycomed Innovations Inc. developed[172] a family of trityl radicals (TAMs) (Figure 15c) bearing 12 sulfur atoms. These are analogues of triphenyl methyl radicals and have been synthesized on a large-scale and used for a variety of EPR oximetry applications.[173−175] TAMs offer a single sharp line

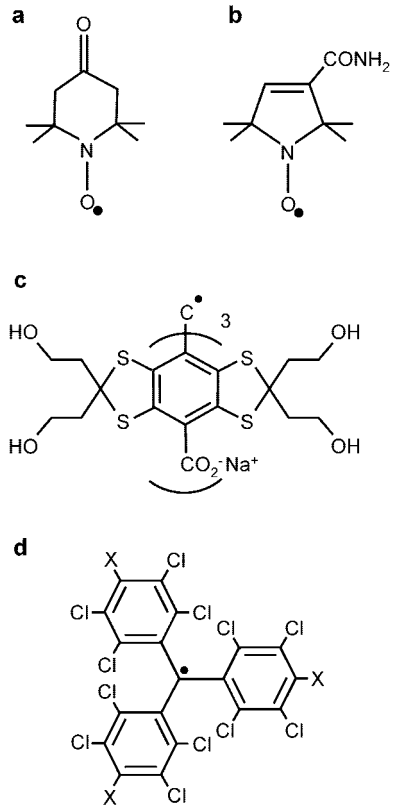

Figure 15. Chemical structure of soluble spin probes commonly used for EPR oximetry. (a) Tempone (1-oxyl-2,2,6,6-tetramethyl-4-piperidione), (b) CTPO (2,2,5,5-tetramethyl-3-pyrroline-1-oxyl-2-carboxamide), (c) TAM (triarylmethyl) OX063, and (d) PTM (perchlorotriphenylmethyl) for X = Cl, PTM-TE for X = COOR, and PTM-TC for X = COOH.

shape and an order-of-magnitude improvement in SNR over other commonly used soluble spin probes. Recently, the synthesis of other derivatives of TAMs has also been reported.[176−178] Perchlorotriarylmethyl (PTM) radicals (Figure 15d) constitute another important trityl type radical used for EPR oximetry. Perchlorotriphenylmethyl triester radical (PTM-TE) was synthesized, as outlined in Scheme 1, by a facile 3-step synthesis[179] using Friedal−Crafts reaction of tetrachlorobenzene with chloroform followed by ethoxycarbonylation and subsequent oxidation. Bratasz et al.[180] reported on the development of an injectable spin probe formulation, consisting of PTM-TE radical dissolved in HFB, for in vivo oximetry and imaging of oxygen concentration in tissues. PTM-TE was evaluated for its oxygen sensitivity, biostability, and distribution in a radiation-induced fibrosarcoma (RIF-1) tumor transplanted into C3H mice. Some of the favorable features of the spin probe are a single narrow EPR peak (anoxic line width, 410 mG), high solubility in HFB (>12 mM), large line width sensitivity to molecular oxygen (∼17 mG/mmHg), good stability in tumor tissue (half-life, 3.3 h), absence of spin−spin broadening (up to 12 mM), and lack of power saturation effects (up to 200 mW).

6.1.2. Particulate Spin Probes

The main advantages of particulate spin probes include high spin density, which leads to high SNR; higher sensitivity to oxygen; and long-term in vivo stability. Particulate spin probe-based oximetry is ideal for making repeated measurements over an extended duration in live animals. A wide array

Scheme 1. Synthesis of PTM-TE Radical[a]

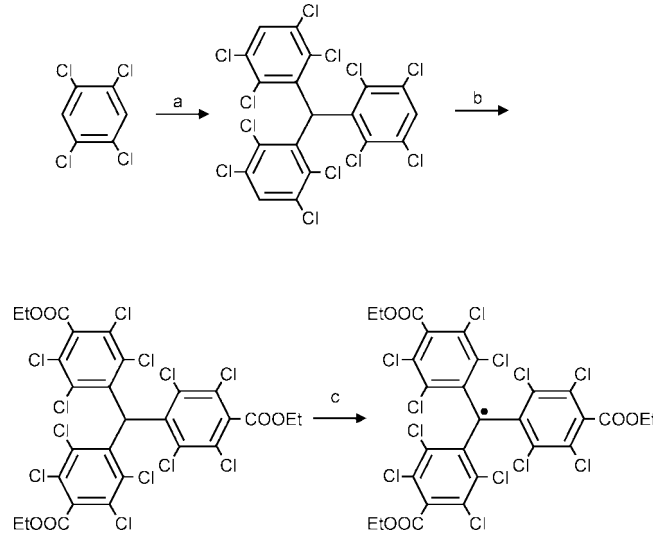

[a] Reagents and conditions: (a) $CHCl_3$, $AlCl_3$. (b) *n*-BuLi, TMEDA, ethyl chloroformate, 77%. (c) (1) NaOH, DMSO/Et_2O; (2) I_2, Et_2O, 93%.

of naturally occurring, semisynthetic, and synthetic particulate spin probes have been developed for EPR oximetry.

Carbon-based materials including coals (such as funinite[161,181] and gloxy[163]), chars[182,183] (either prepared from coals or synthesized from carbohydrates, wood, or other materials), and carbon black[184] (India Ink) have been extensively used for in vivo EPR oximetry. Thus far, India Ink remains the only spin probe approved for in vivo clinical use, in both the United States and Europe. In fact, EPR oximetry using India Ink has already been reported on human subjects.[95] Despite a strong EPR signal and easy availability, poor oxygen sensitivity (charcoals), broad line shape (India Ink), nonlinear relationship between line width and pO_2 (almost all carbon-based particulate spin probes), lack of quality control (coals), poor stability (chars), and presence of nonparamagnetic components in the spectrum (almost all carbon-based particulate spin probes) may render carbon-based particulate spin probes an unattractive option for in vivo applications.

Lithium phthalocyanine (LiPc) (Figure 16a) was the first synthetic particulate molecule to be extensively investigated for biological applications.[156] LiPc is synthesized by electrochemical oxidation of Li_2Pc.[185−187] The EPR spectrum of LiPc is characterized by a single line shape with an anoxic line width of ∼20 mG. LiPc has been studied for long-term in vivo oximetry measurements.[188] The shortcomings of LiPc are saturation at lower power, lack of quality control, a nonlinear relationship between line width and pO_2, and lack of long-term stability in tissues.[156] Recently, derivatives of LiPc, such as phenoxy-substituted LiPc (lithium 1,8,15,22-tetraphenoxyphthalocyanine, LiPc-α-OPh), shown in Figure 16a, have been developed[158] using electrochemical methods. As compared to LiPc, the derivative LiPc-α-OPh shows improved linearity of line width vs pO_2 curve, higher oxygen sensitivity, and improved stability for in vivo applications. The schematic for LiPc-α-OPh synthesis is given in Scheme 2.

Another synthetic crystalline spin probe, lithium naphthalocyanine[159] (LiNc), shown in Figure 16b, has been widely studied for EPR oximetry applications. The LiNc shows higher spin density, a broader range of linear response to oxygen partial pressure, and more favorable power saturation properties when compared to LiPc.[189] However, the chemical properties of LiNc limit its attractiveness for biological

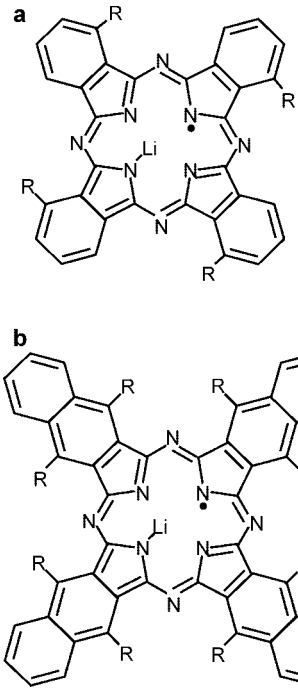

Figure 16. Chemical structure of particulate spin probes commonly used for EPR oximetry. (a) LiPC for R = H and LiPc-α-OPh for R = phenoxy. (b) LiNc for R = H and LiNc-BuO for R = $O(CH_2)_3CH_3$.

Scheme 2. LiPc-α-OPh Was Synthesized by Cyclotetramerization of 3-Phenoxyphthalonitrile (i) in the Presence of Lithium Pentoxide To Obtain Li_2Pc-α-OPh (ii) Followed by Electrochemical Oxidation To Form Microcrystals of LiPc-α-OPh (iii)

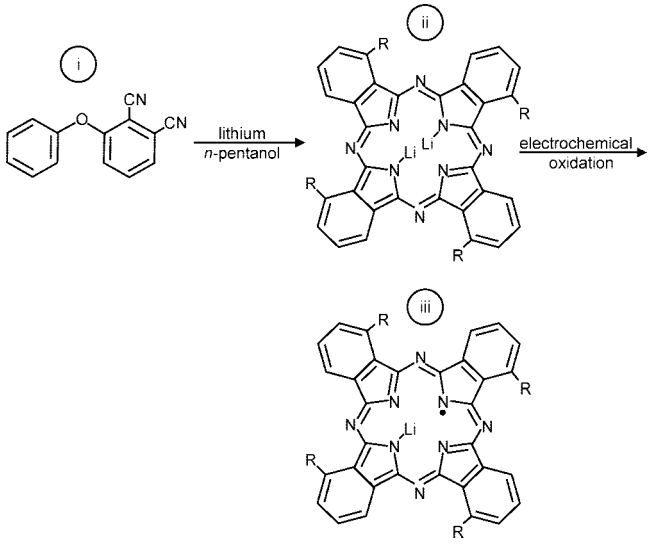

oximetry applications. First of all, it is difficult to synthesize this material in a pure form, and second, it has shown limited stability and responsiveness in tissues.[189] Recently, Pandian et al.[190] have reported an improved chemical procedure to synthesize LiNc crystals in pure form with sustained oxygen sensitivity in tissues. The schematic for LiNc synthesis is shown in Scheme 3.

In efforts to develop better spin probes for EPR oximetry, Pandian et al.[160] reported the preparation of a new derivatized radical, lithium 5,9,14,18,23,27,32,36-octa-*n*-butoxy-2,3-naphthalocyanine (LiNc-BuO). Synthesis for LiNc-BuO is shown in Scheme 4. The spin probe was synthesized[191] from lithium metal and Nc-BuO in *n*-pentanol. The metal-free

Scheme 3. LiNc Was Synthesized by Cyclotetramerization of 2,3-Dicyano Naphthalene (i) in the Presence of Lithium/ Pentanol To Give Li_2Nc (ii) Followed by Oxidation To Form Microcrystals of LiNc (iii)

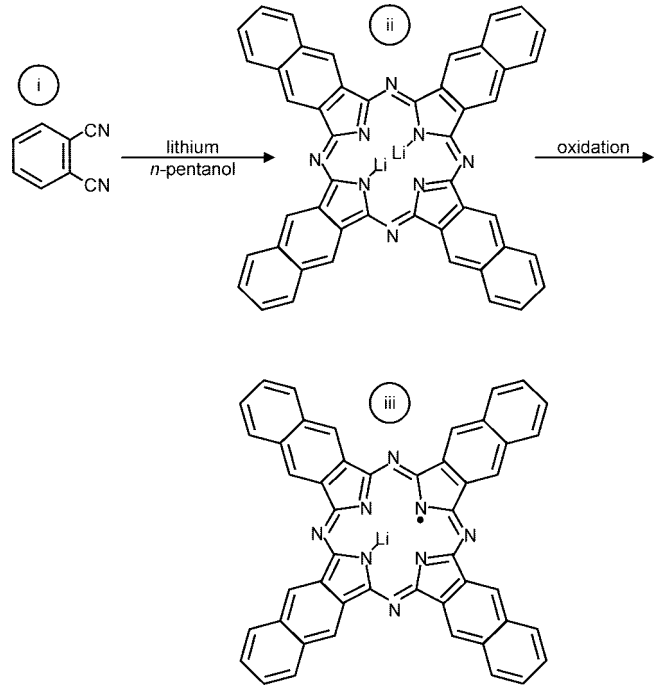

octa-*n*-butoxy-substituted naphthalocyanine (Nc-BuO) macrocyclic ligand readily reacted with lithium pentoxide to give dilithium octa-*n*-butoxy-naphthalocyanine (Li_2Nc-BuO), followed by oxidation to give LiNc-BuO radical, which formed as needle-shaped, dark-green microcrystals, 5−10 μm in diameter and 50−150 μm in length. Preliminary studies of this material showed that the spin probe was stable in tissues and responsive to O_2 for more than 6 months.[160]

The crystal structure of LiNc-BuO contains strongly coupled dimers of LiNc-BuO molecules, which favors a high degree of spin exchange and results in a single sharp EPR line. The molecular packing leads to a structure with open channels large enough (10 × 6 Å^2) for the penetration of small diatomic paramagnetic molecules such as oxygen (O_2) and nitric oxide (NO), as well as the larger triatomic molecules such as nitrogen dioxide (NO_2). The EPR line width of LiNc-BuO is extremely sensitive to the concentration of paramagnetic gases in the pressure range of 0−760 mmHg. The effect of oxygen on LiNc-BuO is reversible without any signs of permanent adsorption or chemical oxidation. The time response of the effect of oxygen is extremely rapid (0.24 s). The paramagnetic gas-sensing properties of LiNc-BuO are attributed to the open molecular framework of the crystal structure. The oxygen sensitivity curves of LiNc and LiNc-BuO are shown in Figure 17. Photographs of a LiNc-BuO microcrystal and stacking of LiNc-BuO molecules within the microcrystal are shown in Figure 18.

6.2. Particulate Spin Probe Encapsulation

The particulate spin probes can be used in their crystalline form to sense molecular oxygen[94] but may have limitations associated with particle migration within the tissue and, potentially, with biocompatibility and chemical toxicity of particles directly exposed to tissue. Exposure of some spin probes to the in vivo environment degrades their oximetry properties over time.[156,189] Successful transformation of EPR

Scheme 4. LiNc-BuO Was Synthesized from Lithium Metal and Octa-*n*-butoxy-Substituted Naphthalocyanine (Nc-BuO) (i) in *n*-Pentanol To Give Dilithium octa-*n*-butoxy-naphthalocyanine (Li_2Nc-BuO) (ii) Followed by Oxidation To Give LiNc-BuO Radical (iii)

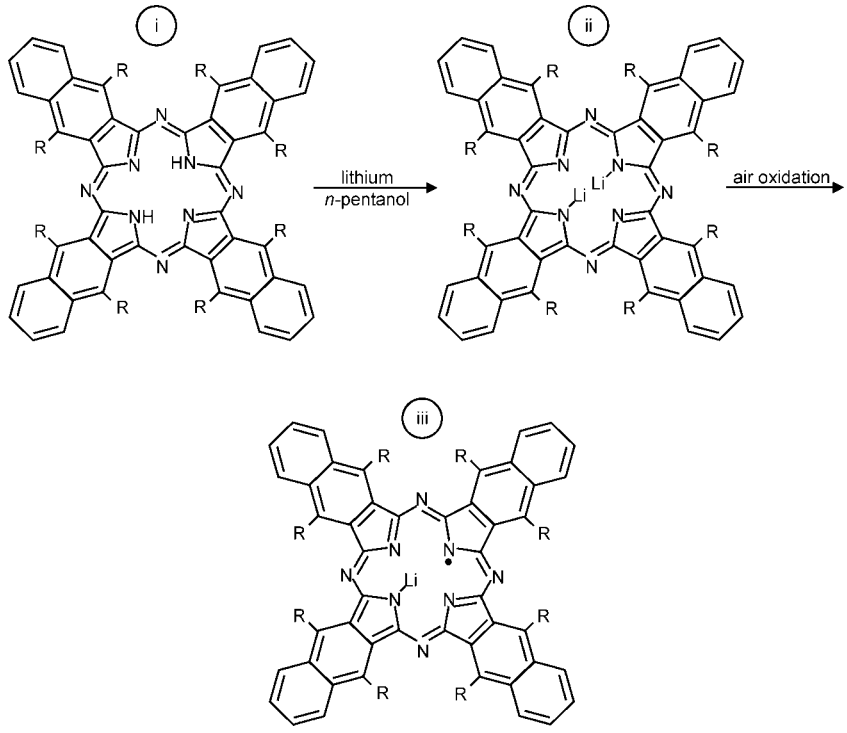

oximetry into a powerful clinical tool requires long-term stabilization of the spin probes in tissue sites, protection of the spin probes from degradative conditions, and insulation between the spin probe and tissue to avoid potential chemical toxicity.

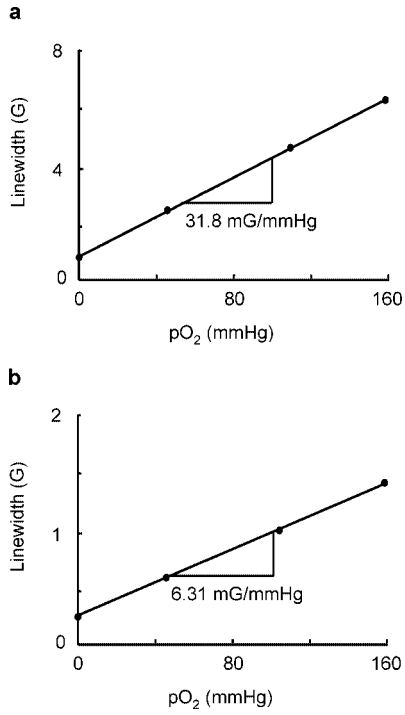

Figure 17. Effect of molecular oxygen on the EPR line width of LiNc (a) and LiNc-BuO (b) crystals. A linear variation of line width with the pO_2 is observed for both of the probes. For LiNc: anoxic linewith, 0.90 G; oxygen sensitivity, 31.8 mG/mmHg. For LiNc-BuO: anoxic line width, 0.41 G; oxygen sensitivity, 6.31 mG/mmHg. Measurements were conducted at the L-band CW EPR spectrometer. The instrumental settings were as follows: microwave power, 2 mW; modulation amplitude, 200 mG; modulation frequency, 100 kHz; receiver time constant, 10 ms; and acquisition time, 10 s (single scan).

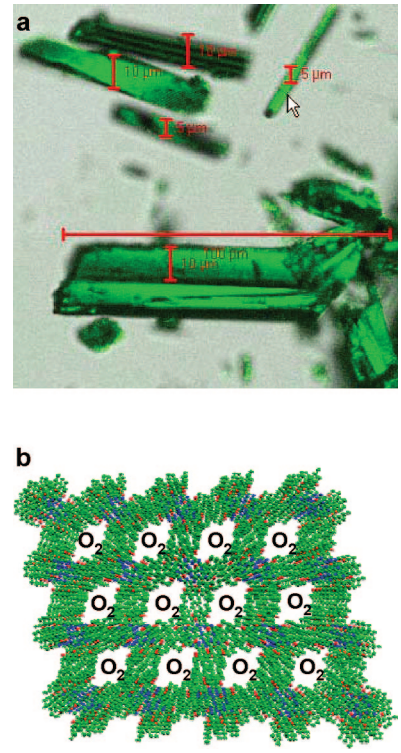

Figure 18. LiNc-BuO in crystalline form. (a) Photograph of needle-shaped LiNc-BuO microcrystals. (b) Stacking of LiNc-BuO molecules in a crystal. The EPR line broadening occurs due to the diffusion of O_2 into the microchannels and subsequent spin−spin interaction through the Heisenberg exchange mechanism. Image b is reprinted with permission from ref 191. Copyright 2006 The Royal Society of Chemistry. DOI: 10.1039/b517976a.

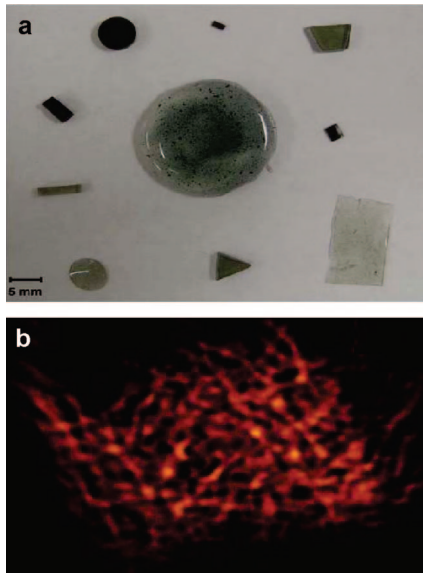

Figure 19. Chips fabricated by the encapsulation of LiNc-BuO particulates in PDMS. (a) Pieces of polymerized LiNc-BuO with varying sizes, shapes, and ratios of particulate to polymer. The dark shade indicates a higher concentration of LiNc-BuO crystals. (b) X-band EPR images of polymerized LiNc-BuO chip to evaluate spin distribution. Samples were imaged under anoxic conditions in a sealed tube. Reprinted with permission from ref 196. Copyright 2009 Springer.

Several studies have approached this set of challenges by encapsulating crystalline spin probes in biocompatible, biostable, gas-permeable polymer matrices.[192−195] Some critical parameters that need to be considered in the development of encapsulated oximetry spin probes include the cost of the encapsulating polymer, in vivo stability (mechanical and chemical) of the polymer material, and film oxygen permeability.

In the past, coating of carbon-based particulate spin probes using a number of biopolymers[13] has been reported. Encapsulation of LiPc using Teflon AF 2400 (TAF), cellulose acetate, and polyvinyl acetate has also been reported. The coating of LiPc using TAF was performed by solvent evaporation approaches, which produced very thin TAF films.[193] While the oximetry properties of TAF-encapsulated LiPc were encouraging, the handling properties of the films were inconvenient. Thin TAF films were brittle, and maintaining them intact during implantation and explantation was challenging. Thick, multilayer TAF encapsulation of oximetry particles was not feasible, because of the low solubility of TAF in the available solvents.

To overcome these operational difficulties, Meenakshisumdaram et al.[196] recently proposed a simple and easy-to-use cast-molding and polymerization method, using polydimethylsiloxane (PDMS), which allowed for the fabrication of mechanically robust spin probe encapsulations. PDMS is a biocompatible, highly flexible, and highly oxygen permeable silicone polymer that has been used in a wide range of medical device and health care applications. Also, PDMS has been approved for use in human subjects and is one of the reference materials provided by the National Heart Lung and Blood Institute for standardized biocompatibility testing.[197] The method also provided the capability of covering the embedded oximetry crystals with multiple layers of PDMS for fully sequestering them from the in vivo environment and improving their biotolerability. Figure 19 shows chips fabricated by the encapsulation of LiNc-BuO particulates in PDMS.

7. Applications of EPR Oximetry

EPR oximetry has been used extensively for cellular studies to measure intracellular and extracellular oxygen concentrations, oxygen consumption rate, and membrane permeability and structure.[11] It has also been developed as a powerful tool for localized measurements of oxygen in organs and tissues, which is extremely helpful in investigating various physiological and pathophysiological conditions. Several studies have been conducted using EPR oximetry to measure oxygen in the brain, heart, gastrointestinal tract, skeletal muscle, liver, kidneys, skin, and other organs.[94] Because of limited penetration depth, the existing EPR techniques are restricted to studies involving small animals or topical regions of large animals. In this section, a few important applications of EPR are briefly discussed.

7.1. In Vitro Applications

One of the early applications of EPR oximetry was to measure the oxygen consumption rate in tumor cell suspensions.[198,199] Two models, closed-chamber and open-chamber, were developed. In the closed-chamber model, the sample was isolated from the surrounding using oxygen impermeable medium. The oxygen consumption rate was quantified by measuring the overall oxygen concentration as a function of time in the sample. In the open-chamber model, the oxygen consumption rate was quantified by measuring the amount of oxygen diffusing through an oxygen permeable membrane, such as Teflon or methyl pentene polymer,[152] separating the sample from the surroundings. Recently, EPR oximetry has also been shown to successfully monitor the intracellular and extracellular oxygen simultaneously by using two different spin probes.[174,200] One spin probe was internalized in the cells and reported the intracellular pO_2, while other particulate spin probes stayed outside and reported the extracellular pO_2 values.

EPR oximetry has also been applied to study oxygen transportation both across and within a lipid bilayer model membrane.[90] This method was used to obtain profiles of oxygen transport parameter, which, in turn, were used to evaluate the oxygen permeability coefficient of the membrane.[91] In addition, oxygen transport parameter profiles have also been used to study membrane structure. The DOT method[201] (method of discrimination by oxygen transport), for instance, was effectively used to indicate the existence of lipid domains that exhibit slow oxygen transport rate. EPR oximetry has also been utilized to study the effects of membrane modifiers such as cholesterol,[202] carotenoids,[203] and transmembrane α-helical peptides[204] on oxygen transportation across the membrane. A book chapter by Subczynski and Swartz[11] treats the topic of in vitro EPR oximetry applications in detail.

7.2. In Vivo Applications

In vivo EPR oximetry applications generally include the study of oxygenation of several tissues and organs under various pathophysiological conditions. Exciting in vivo applications of EPR oximetry have emerged in the last two decades, but continuous development of oxygen-sensitive spin probes coupled with technical advancements in the

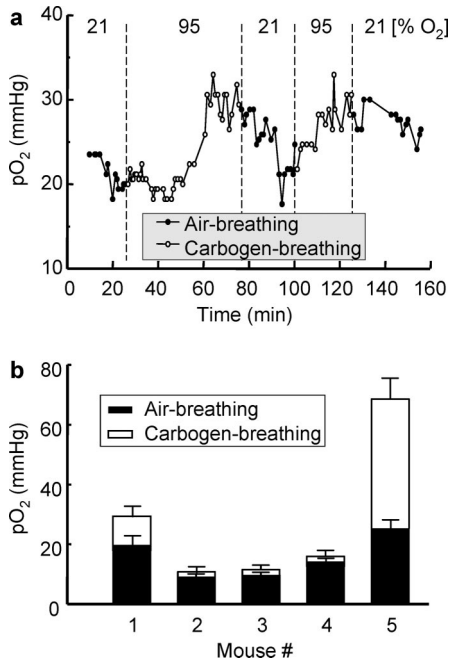

Figure 20. Effect of FiO_2 (fraction of inspired oxygen) on the tumor pO_2. Twenty microliters of PTM-TE (12 mM in HFB) was injected directly into RIF-1 tumor grown in the hind leg of a C3H mouse. (a) Change in pO_2 in the tumor of a single animal, while the FiO_2 was successively switched between 21 and 95% (carbogen gas), as indicated. (b) The pO_2 values obtained before ($FiO_2 = 21\%$) and 20 min after changing the FiO_2 to 95% in five different animals. Reprinted with permission from ref 180. Copyright 2007 Elsevier.

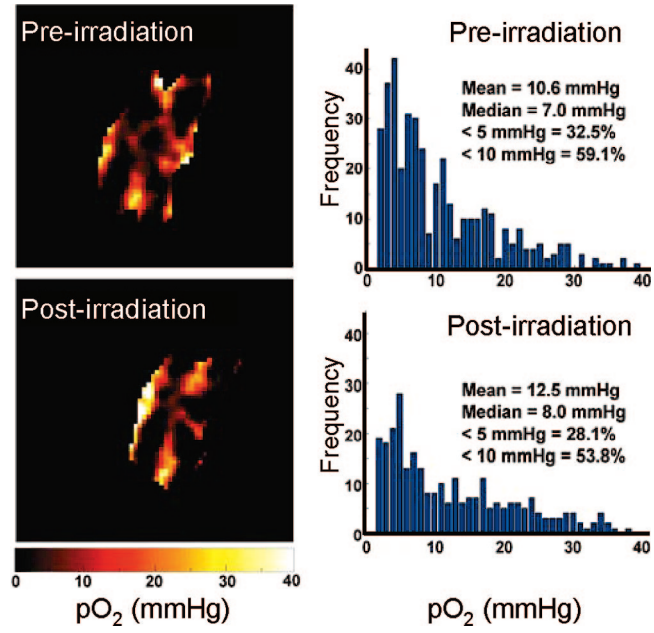

Figure 21. In vivo mapping of tumor pO_2 during growth and after treatment with X-ray irradiation. Change and redistribution of tumor pO_2 are shown for a small (113 mm^3) RIF-1 tumor before (pre-) and 1 h after (post-) X-ray irradiation. The tumor was implanted with RIF-1 cells internalized with nanoparticulates of LiNc-BuO. A dose of 30 Gy was delivered with 6 MeV electrons at a dose rate of 3 Gy/min. Redistribution is seen with a modest increase in the pO_2. Reprinted with permission from ref 213. Copyright 2007 John Wiley and Sons.

instrumentation promises that more applications will follow. Here, we visit some of the widely studied in vivo applications of EPR oximetry.

7.2.1. Cancer/Tumor Applications

Tumor hypoxia is strongly linked to poor treatment outcome from chemo- or radiotherapy in several human malignancies.[205] Hypoxic tumors are biologically more aggressive, and it has been reported that hypoxic sarcoma or cervical cancers[27,206] tend to metastasize faster. More recently, it has also been reported[207] that ovarian cancer cells grown in a hypoxic environment tend to be more resistant to common chemotherapies than the cancer cells grown under normoxia. The fact that poorly oxygenated tumors are more aggressive and less susceptible to treatment suggests that tumor oxygenation status is an important parameter for cancer treatment.[208] The observation of substantial inter- and intratumor heterogeneities among tumors of similar histology and sites further emphasizes the importance of the measurement of hypoxia in individual tumor patients. The ability to monitor changes in the pO_2 before and after treatment could have profound implications for the planning of effective therapeutic strategies.[209] In particular, radiotherapy could benefit from modulated treatment based on regional variations in pO_2.

While these tumor oximetry studies demonstrate the clinical potential of in vivo oximetry, they also point to the limitations of commonly employed oximetry methods. For instance, measurements involving electrodes are highly invasive and cannot be used for repeated measurements from the same site, and measurements using PET involve exposure to ionizing radiation. EPR oximetry avoids some of the important limitations associated with other methods. It is a minimally invasive method that allows for repeated measurements and possesses high sensitivity to in vivo oxygen levels. Elas et al.[173] conducted a comparative study quantitatively correlating EPR oximetry using a trityl spin probe with OxyLite-based oximetry.

Halpern et al.[210] conducted spectral-spatial imaging, in one spatial dimension, to provide a quantitative map of pO_2 distribution across the tumor using a soluble spin probe. In another study,[211] the same group examined the affect of breathing in PFC/carbogen on the oxygenation of fibrosarcomas. Gallez et al.[153] used nitroxides for assessing perfusion, oxygenation, and viability of tissues in murine tumor models. Krishna et al.[150] reported coregistration of tumor anatomy with pO_2 distribution using OMRI. Bratasz et al.[180] reported the development of an injectable spin probe formulation, consisting of PTM-TE radical dissolved in HFB for in vivo oximetry under two different breathing environments. These results are summarized in Figure 20.

EPR oximetry employing particulate spin probes has also been used extensively to measure murine tumor oxygenation. Particulate spin probes are more suitable for long-term measurements and require one-time implantation at one or more locations in the region of interest. Measurements over several days or weeks enable the tracking of tumor oxygenation. Goda et al. studied changes in oxygen tension in experimental tumors, RIF-1 tumors, and mouse mammary tumor (MTG-B) after a single dose of X-ray irradiation. Ilangovan et al.[212] reported pO_2 mapping of tumors by coimplanting LiPc particulates with RIF-1 cells subcutaneously in the murine leg. Spectral-spatial imaging can be performed to map the spatial distribution of oxygen concentration in a tumor. Using a similar model, Bratasz et al.[213] conducted studies using LiNc-BuO to report pO_2 maps before and after a single dose of 30 Gy X-ray irradiation. The results

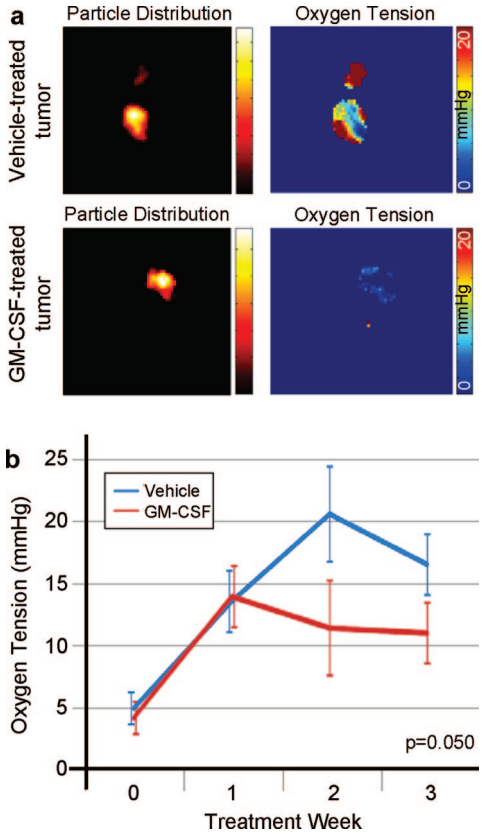

Figure 22. Intratumor GM-CSF treatment reduces oxygen levels within mammary tumors in vivo. (a) Representative EPR images showing probe distribution (left) and oxygen in the tumor (right). (b) Trends in tumor oxygen levels over time (±SEM, $N = 5$). Reprinted with permission from ref 215. Copyright 2009 American Association of Cancer Research.

are summarized in Figure 21. Hou et al.[214] have investigated the temporal effects of single or fractionated radiotherapy on subcutaneous RIF-1 tumor using multisite oximetry.[144] The purpose of the study was to determine the therapeutic outcomes when the timing of fractionations is guided by tumor pO_2. In another interesting study, the role of granulocyte-macrophage colony-stimulating factor (GM-CSF) in the inhibition of breast cancer growth has been studied using EPR oximetry.[215] Figure 22 shows the effect of GM-CSF on tumor size. Murine tumor oximetry using encapsulated particulate spin probes has also been reported.[216,217] A review article by Gallez et al.[218] provides a well-rounded account of EPR tumor oximetry.

7.2.2. Cardiac Applications

Fluctuations in free radical generation, oxygenation, and nitric oxide concentration carry importance in a variety of cardiovascular diseases. Cardiac oximetry imposes a great technical challenge due to cardiac motion. EPR oximetry in isolated perfused rat hearts has been demonstrated.[110,219] Studies have also been conducted for isolated beating heart[16,220] and heart in situ models,[221] with both soluble and particulate spin probes.

Grinberg et al.[222] reported measurements of myocardial pO_2 by EPR oximetry in an isolated perfused rat heart during treatment with different cardioactive drugs: dobutamine, metoprolol, verapamil, vasopressin, and Nω-nitro-L-arginine methyl ester. The relationship of oxidative damage associated with ischemia/reperfusion (I/R) injury and the amount of oxygen in the heart have been the focus in several studies.

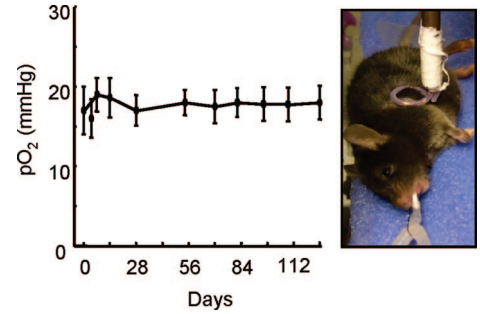

Figure 23. Long-term monitoring of in situ pO_2 at the site of transplanted SM in infarcted mouse hearts. Myocardial tissue pO_2 from mice ($N = 5$) implanted with LiNc-BuO in the midventricular region without left anterior descending coronary artery ligation. Data show the feasibility of pO_2 measurements for more than 3 months after implantation. Reprinted with permission from ref 226. Copyright 2008 Springer.

Ilangovan et al.[16] studied the myocardial oxygen consumption rate as an index of postischemic recovery. Angelos et al.[223] studied the effect of hypoxic reperfusion and subsequent reactive oxygen species (ROS) generation on cardiac function using EPR oximetry.

EPR oximetry has also been used to investigate the efficacy of various treatment options, including ischemic preconditioning and ROS-scavenging (antioxidant) drugs. For instance, studies by Zhu et al.[224] reported that ischemic preconditioning attenuated in vivo postischemic myocardial hyperoxygenation by improving myocardial oxygen consumption and decreasing ROS or reactive nitrogen species generation after regional I/R. Another recent study[225] showed that sulfaphenazole (SPZ) protected the hearts from I/R injury. The overall aim of this study was to investigate the cardioprotective effect of SPZ and to delineate the involvement of NO, superoxide, and oxygenation and also to establish the signaling mechanism involved in cardioprotection in an in vivo rat model of acute myocardial infarction (MI). The beneficial effect, measured by hemodynamic functionality, correlated with a significant elevation of tissue oxygenation and bioavailability of NO.

Several recent studies utilized EPR oximetry to investigate the efficacy of stem cell therapy for treating MI. Khan et al.[226] reported noninvasive long-term monitoring of in situ pO_2 during engraftment of stem cells in the infarct heart. Figure 23 displays the in situ oximetry data collected for over 3 months from a mouse heart transplanted with skeletal myoblasts (SM) using LiNc-BuO as a spin probe. In a separate but related study,[227] the same author compared the oxygenation of infracted myocardial tissue with and without transplantation of SM. The myocardial pO_2 at the site of SM cell therapy was significantly higher when compared to the untreated group throughout the 4 week period as shown in Figure 24. The increased myocardial pO_2 positively correlated with neoangiogenesis and cardiac function.

In another study by Chacko et al.,[228] bone marrow-derived mesenchymal stem cells (MSC) were transplanted in the infarct heart of rats and showed significant reduction of infarct size followed by substantial recovery of tissue oxygenation, neovascularization, and cardiac function. In a recent report, Khan et al.[229] investigated the effect of hyperbaric oxygenation (HBO) on the engraftment of bone marrow-derived rat MSCs transplanted in infarct rat hearts. HBO (100% oxygen at 2 ATA for 90 min) was administered daily for 2 weeks. The results showed (Figure 25) an increase

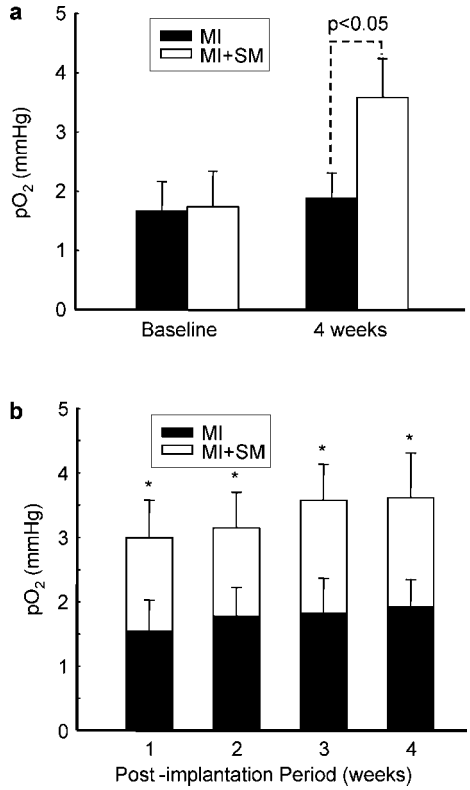

Figure 24. Myocardial pO_2 in the infarcted heart at the site of cell transplantation. Myocardial pO_2 values were measured repeatedly for 4 weeks using in vivo EPR oximetry in mice hearts transplanted with LiNc-BuO-labeled SM cells. (a) Tissue pO_2 at 4 weeks after treatment with SM cells (MI + SM) was significantly higher as compared to untreated (MI) hearts. (b) The time course values of myocardial pO_2 measured from infarcted hearts (MI) and infarcted hearts treated with SM cells (MI + SM) are shown. Values are expressed as means ± SDs ($n = 7$ per group). *$p < 0.05$ vs MI group. Reprinted with permission from ref 227. Copyright 2007 American Physiological Society.

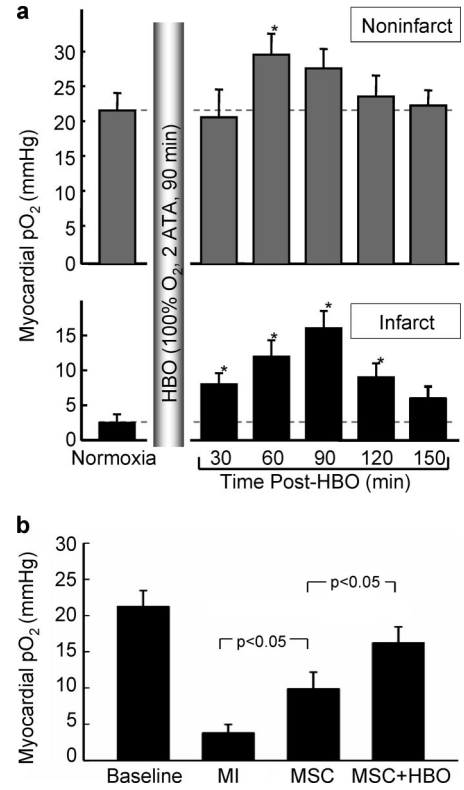

Figure 25. HBO and myocardial pO_2, in vivo. (a) Myocardial pO_2 in (noninfarcted and infarct) rat hearts measured before (normoxia) and after HBO. Data represent means ± SDs obtained from four rats. The results show an increase in oxygenation levels reaching significance at 60 min followed by returning to baseline in about 2.5 h in the noninfarcted hearts. In the infarcted hearts, the oxygenation levels are significantly higher up to 2 h post-treatment. It is interesting to note that a 5.8-fold increase in oxygenation is achieved in the infarct hearts after 90 min of HBO. (b) Myocardial pO_2 in rat hearts transplanted with stem cells at 2 weeks. The results (means ± SDs; $N = 4$ rats) show an increase in myocardial oxygenation in hearts treated with MSC, and further enhancement in pO_2 was observed in hearts treated with HBO. Reprinted with permission from ref 229. Copyright 2009 Elsevier.

in oxygenation levels reaching significance at 60 min followed by a return to baseline in about 2.5 h after the conclusion of HBO application in the noninfarcted hearts. Elevated oxygen levels were, however, sustained for more than 2 h after the HBO administration in the infarcted heart. The results suggested that HBO treatment restored myocardial oxygenation to near normal levels in the infarct heart transplanted with MSCs.

7.2.3. Wound Healing Applications

Oxygen measurement in skin and other immediately underlying tissues is critical for evaluating the condition and treatment options for topical wounds, burns, and peripheral vascular disease. For these applications, where penetration depth is generally not a deciding factor, EPR oximetry holds a lot of promise for large animal models and potential clinical applications involving humans.

At the wound site, vasculature disruption leads to localized hypoxia.[230] Interestingly, both hypoxia and hyperoxia, when present in moderation, have been known to induce angiogenesis,[231] which plays a critical role in wound healing. However, hypoxia and hyperoxia, when present in the extreme, can derail tissue repair. Extreme hypoxia is unable to promote or sustain the growth of functional blood vessels. Extreme hyperoxia, on the other hand, can cause oxygen toxicity, which can adversely affect the healing process. Oxygen therapy is commonly used in the wound clinics to treat wound hypoxia.[232] Schugart et al.[233] developed a mathematical model for addressing the role of tissue oxygenation on cutaneous wound healing. In a recent study, Lu et al.[234] studied decreases in oxygen levels due to tibial fracture.

Oxygen measurements also provide useful insight into the status, progression, and treatment of peripheral vascular diseases such as diabetic foot. Studies using this technique have been carried out in volunteers using India Ink and whole body clinical EPR instruments, and encouraging results have been reported.[95]

7.2.4. Application of EPR Oximetry to Other Organs

EPR oximetry has also been studied for in vivo measurements in other organs and tissues such as liver, brain, kidney, and skeletal muscle. Numerous studies, using EPR oximetry, have reported oxygen levels in the medulla and cortex of isolated perfused[163] and in vivo[235] kidney models. A number of pathophysiological conditions can affect liver pO_2. EPR oximetry also has been used to study localized pO_2 in liver.[164,236] The value of pO_2 is known to affect the energetics of muscle function. EPR oximetry has been applied to study oxygenation of skeletal muscle.[237] The brain is quite vulner-

able to pO_2 fluctuations. Several studies[238,239] show that EPR has been successfully used in small animal models to monitor brain oxygen over an extended duration of time. In addition, EPR oximetry has been used to evaluate the relationship between elevated levels of tissue pO_2 and healing of radiation-damaged tissues.

8. Conclusions

The measurement of oxygen in biological samples, especially in vivo, has been of paramount interest. Several techniques have been developed for in vivo oxygen measurement, but no single technique has fully established itself for broad applications. EPR oximetry, due to its minimally invasive nature, capability to measure absolute pO_2, high sensitivity to oxygen, and ability to make repeated measurements, has emerged as a method of choice for a wide array of biological applications. In recent years, the number of laboratories and research groups contributing to the development of EPR oximetry has increased. Significant strides have been made in spin probe synthesis and encapsulation, instrumentation development, and algorithm development for data collection and processing. Despite all of the progress, translation of EPR oximetry to broad clinical applications has been hindered by lack of SNR at low frequencies, long acquisition times, and lack of FDA-approved spin probes suitable for implantation. Considering the progress made in the past decade, however, realization of clinical applications of EPR oximetry, especially for oncology, peripheral vascular disease, and wound healing, seems only a few strides away.

9. Acknowledgments

We acknowledge the support of the National Institutes of Health for providing funding for several EPR-related research projects, including EB004031. We also thank Brian Rivera for proofreading.

10. References

(1) Lane, N. *Oxygen: The Molecule That Made the World*; Oxford University Press: Oxford, 2002.
(2) Falkowski, P. G. *Science* **2006**, *311*, 1724.
(3) Jiang, Y. Y.; Kong, D. X.; Qin, T.; Zhang, H. Y. *Biochem. Biophys. Res. Commun.* **2009**, *391*, 1158.
(4) Raymond, J.; Segre, D. *Science* **2006**, *311*, 1764.
(5) Kulkarni, A. C.; Kuppusamy, P.; Parinandi, N. *Antioxid. Redox Signaling* **2007**, *9*, 1717.
(6) Prabhakar, N. R.; Kumar, G. K.; Nanduri, J.; Semenza, G. L. *Antioxid. Redox Signaling* **2007**, *9*, 1397.
(7) Sieck, G. C. *J. Appl. Physiol.* **2004**, *96*, 375.
(8) Dewhirst, M. W.; Klitzman, B.; Braun, R. D.; Brizel, D. M.; Haroon, Z. A.; Secomb, T. W *Int. J. Cancer* **2000**, *90*, 237.
(9) Swartz, H. M.; Dunn, J. F. *Adv. Exp. Med. Biol.* **2003**, *530*, 1.
(10) Hunt, T. K.; Rabkin, J.; Jensen, J. A.; Jonsson, K.; Smitten, K. V.; Goodson, W. H. *World J. Surg.* **1987**, *11*, 126.
(11) Subczynski, W. K.; Swartz, H. M. In *Biomedical EPR, Part A: Free Radicals, Metals, Medicine, and Physiology*; Eaton, S. R., Eaton, G. R., Berliner, J. L., Eds.; Kluwer Academic/Plenum Publisher: New York, 2005.
(12) Dunn, J. F.; Swartz, H. M. *Methods* **2003**, *30*, 159.
(13) Gallez, B.; Jordan, B. F.; Baudelet, C. *Magn. Reson. Med.* **1999**, *42*, 193.
(14) Gallez, B.; Jordan, B. F.; Baudelet, C.; Misson, P. D. *Magn. Reson. Med.* **1999**, *42*, 627.
(15) O'Hara, J. A.; Goda, F.; Demidenko, E.; Swartz, H. M. *Radiat. Res.* **1998**, *150*, 549.
(16) Ilangovan, G.; Liebgott, T.; Kutala, V. K.; Petryakov, S.; Zweier, J. L.; Kuppusamy, P. *Magn. Reson. Med.* **2004**, *51*, 835.
(17) Severinghaus, J. W. *The History of Anesthesia*, Proceedings of the Fifth International Symposium on the History of Anesthesia; Elsevier: Santiago, Spain, 2001; p 115.
(18) Cater, D. B.; Silver, I. A. *Acta Radiol.* **1960**, *53*, 233.
(19) Kolstad, P. *Scand. J. Clin. Lab. Invest. Suppl.* **1968**, *106*, 145.
(20) Hockel, M.; Schlenger, K.; Knoop, C.; Vaupel, P. *Cancer Res.* **1991**, *51*, 6098.
(21) Brizel, D. M.; Scully, S. P.; Harrelson, J. M.; Layfield, L. J.; Dodge, R. K.; Charles, H. C.; Samulski, T. V.; Prosnitz, L. R.; Dewhirst, M. W. *Cancer Res.* **1996**, *56*, 5347.
(22) Dewhirst, M. W.; Ong, E. T.; Madwed, D.; Klitzman, B.; Secomb, T.; Brizel, D.; Bonaventura, J.; Rosner, G.; Kavanagh, B.; Edwards, J.; Gross, J. *Radiat. Res.* **1992**, *132*, 61.
(23) Clark, L. C. *Trans. Am. Soc. Artif. Intern. Organs* **1956**, *2*, 41.
(24) Whalen, W. J.; Riley, J.; Nair, P. *J. Appl. Physiol.* **1967**, *23*, 798.
(25) Tsai, A. G.; Friesenecker, B.; Mazzoni, M. C.; Kerger, H.; Buerk, D. G.; Johnson, P. C.; Intaglietta, M. *Proc. Natl. Acad. Sci. U.S.A.* **1998**, *95*, 6590.
(26) Baudelet, C.; Gallez, B. *Magn. Reson. Imaging* **2004**, *22*, 905.
(27) Brizel, D. M.; Scully, S. P.; Harrelson, J. M.; Layfield, L. J.; Bean, J. M.; Prosnitz, L. R.; Dewhirst, M. W. *Cancer Res.* **1996**, *56*, 941.
(28) Okunieff, P.; Ding, I.; Vaupel, P.; Hockel, M. *Adv. Exp. Med. Biol.* **2003**, *510*, 69.
(29) Vaupel, P.; Schlenger, K.; Knoop, C.; Hockel, M. *Cancer Res.* **1991**, *51*, 3316.
(30) O'Hara, J. A.; Khan, N.; Hou, H.; Wilmo, C. M.; Demidenko, E.; Dunn, J. F.; Swartz, H. M. *Physiol. Meas.* **2004**, *25*, 1413.
(31) Huch, A.; Huch, R.; Arner, B.; Rooth, G. *Scand. J. Clin. Lab. Invest. Suppl.* **1973**, *31*, 269.
(32) Rooth, G. *Pediatrics* **1975**, *55*, 232.
(33) Yu, M.; Morita, S. Y.; Daniel, S. R.; Chapital, A.; Waxman, K.; Severino, R. *Shock* **2006**, *26*, 450.
(34) Amann, B.; Luedemann, C.; Ratei, R.; Schmidt-Lucke, J. A. *Cell Transplant* **2009**, *18*, 371.
(35) Hodgkiss, R. J. *Anti-Cancer Drug Des.* **1998**, *13*, 687.
(36) Koch, C. J.; Evans, S. M. *Adv. Exp. Med. Biol.* **2003**, *510*, 285.
(37) Kennedy, A. S.; Raleigh, J. A.; Perez, G. M.; Calkins, D. P.; Thrall, D. E.; Novotny, D. B.; Varia, M. A. *Int. J. Radiat. Oncol. Biol. Phys.* **1997**, *37*, 897.
(38) Griffiths, J. R.; Robinson, S. P. *Br. J. Radiol.* **1999**, *72*, 627.
(39) Wen, B.; Urano, M.; O'Donoghue, J. A.; Ling, C. C. *Radiat. Res.* **2006**, *166*, 512.
(40) Nwaigwe, C. I.; Roche, M. A.; Grinberg, O.; Dunn, J. F. *Adv. Exp. Med. Biol.* **2003**, *530*, 101.
(41) O'Hara, J. A.; Hou, H.; Demidenko, E.; Springett, R. J.; Khan, N.; Swartz, H. M. *Physiol. Meas.* **2005**, *26*, 203.
(42) Jordan, B. F.; Cron, G. O.; Gallez, B. *Magn. Reson. Med.* **2009**, *61*, 634.
(43) Pawlowski, M.; Wilson, D. F. *Adv. Exp. Med. Biol.* **1992**, *316*, 179.
(44) Rumsey, W. L.; Vanderkooi, J. M.; Wilson, D. F. *Science* **1988**, *241*, 1649.
(45) Shibata, M.; Ichioka, S.; Ando, J.; Kamiya, A. *J. Appl. Physiol.* **2001**, *91*, 321.
(46) Vinogradov, S. A.; Lo, L. W.; Jenkins, W. T.; Evans, S. M.; Koch, C.; Wilson, D. F. *Biophys. J.* **1996**, *70*, 1609.
(47) Tsukada, K.; Sakai, S.; Hase, K.; Minamitani, H. *Biosens. Bioelectron.* **2003**, *18*, 1439.
(48) Wilson, D. F.; Vinogradov, S. A.; Grosul, P.; Vaccarezza, M. N.; Kuroki, A.; Bennett, J. *Appl. Opt.* **2005**, *44*, 5239.
(49) DeCampli, W. M.; Schears, G.; Myung, R.; Schultz, S.; Creed, J.; Pastuszko, A.; Wilson, D. F. *J. Thorac. Cardiovasc. Surg.* **2003**, *125*, 472.
(50) Lo, L. W.; Jenkins, W. T.; Vinogradov, S. A.; Evans, S. M.; Wilson, D. F. *Adv. Exp. Med. Biol.* **1997**, *411*, 577.
(51) Wilson, D. F.; Cerniglia, G. J. *Adv. Exp. Med. Biol.* **1994**, *345*, 539.
(52) Severinghaus, J. W. *J. Clin. Monit.* **1986**, *2*, 270.
(53) Walters, T. P. *Br. J. Nurs.* **2007**, *16*, 1332.
(54) Cohn, S. M. *J. Am. Coll. Surg.* **2007**, *205*, 322.
(55) Quaresima, V.; Ferrari, M. *J. Appl. Physiol.* **2009**, *107*, 371.
(56) Thomson, S. J.; Cowan, M. L.; Forton, D. M.; Clark, S. J.; Musa, S.; Grounds, M.; Rahman, T. M *Liver Int.* **2009**, *30*, 463.
(57) Carandang, R.; Krieger, D. W. *Neurocrit. Care* **2007**, *6*, 161.
(58) De Blasi, R. A.; Fantini, S.; Franceschini, M. A.; Ferrari, M.; Gratton, E. *Med. Biol. Eng. Comput.* **1995**, *33*, 228.
(59) Gora, F.; Shinde, S.; Elwell, C. E.; Goldstone, J. C.; Cope, M.; Delpy, D. T.; Smith, M. *J. Neurosurg. Anesthesiol.* **2002**, *14*, 218.
(60) Tamura, M.; Hazeki, O.; Nioka, S.; Chance, B. *Annu. Rev. Physiol.* **1989**, *51*, 813.
(61) Vo-Dinh, T.; Stokes, D. L.; Wabuyele, M. B.; Martin, M. E.; Song, J. M.; Jagannathan, R.; Michaud, E.; Lee, R. J.; Pan, X. *IEEE Eng. Med. Biol. Mag.* **2004**, *23*, 40.
(62) Khoobehi, B.; Beach, J. M.; Kawano, H. *Invest. Ophthalmol. Vis. Sci.* **2004**, *45*, 1464.
(63) Sorg, B. S.; Moeller, B. J.; Donovan, O.; Cao, Y.; Dewhirst, M. W. *J. Biomed. Opt.* **2005**, *10*, 44004.
(64) Zuzak, K. J.; Schaeberle, M. D.; Gladwin, M. T.; Cannon, R. O., 3rd; Levin, I. W. *Circulation* **2001**, *104*, 2905.

(65) Shah, S. A.; Bachrach, N.; Spear, S. J.; Letbetter, D. S.; Stone, R. A.; Dhir, R.; Prichard, J. W.; Brown, H. G.; LaFramboise, W. A. *Biotechniques* **2003**, *34*, 408.
(66) Cancio, L. C.; Batchinsky, A. I.; Mansfield, J. R.; Panasyuk, S.; Hetz, K.; Martini, D.; Jordan, B. S.; Tracey, B.; Freeman, J. E. *J. Trauma* **2006**, *60*, 1087.
(67) Aboagye, E. O.; Kelson, A. B.; Tracy, M.; Workman, P. *Anti-Cancer Drug Des.* **1998**, *13*, 703.
(68) Read, S. J.; Hirano, T.; Abbott, D. F.; Sachinidis, J. I.; Tochon-Danguy, H. J.; Chan, J. G.; Egan, G. F.; Scott, A. M.; Bladin, C. F.; McKay, W. J.; Donnan, G. A. *Neurology* **1998**, *51*, 1617.
(69) Dolbier, W. R., Jr.; Li, A. R.; Koch, C. J.; Shiue, C. Y.; Kachur, A. V. *Appl. Radiat. Isot.* **2001**, *54*, 73.
(70) Chapman, J. D.; Engelhardt, E. L.; Stobbe, C. C.; Schneider, R. F.; Hanks, G. E. *Radiother. Oncol.* **1998**, *46*, 229.
(71) Lehtio, K.; Oikonen, V.; Gronroos, T.; Eskola, O.; Kalliokoski, K.; Bergman, J.; Solin, O.; Grenman, R.; Nuutila, P.; Minn, H. *J. Nucl. Med.* **2001**, *42*, 1643.
(72) Koh, W. J.; Bergman, K. S.; Rasey, J. S.; Peterson, L. M.; Evans, M. L.; Graham, M. M.; Grierson, J. R.; Lindsley, K. L.; Lewellen, T. K.; Krohn, K. A.; Griffin, T. W. *Int. J. Radiat. Oncol. Biol. Phys.* **1995**, *33*, 391.
(73) Busse, L. J.; Thomas, S. R.; Pratt, R. G.; Clark, L. C., Jr.; Ackerman, J. L.; Samaratunga, R. C.; Hoffmann, R. E. *Med. Phys.* **1986**, *13*, 518.
(74) Clark, L. C., Jr.; Ackerman, J. L.; Thomas, S. R.; Millard, R. W.; Hoffman, R. E.; Pratt, R. G.; Ragle-Cole, H.; Kinsey, R. A.; Janakiraman, R. *Adv. Exp. Med. Biol.* **1984**, *180*, 835.
(75) Mason, R. P.; Rodbumrung, W.; Antich, P. P. *NMR Biomed.* **1996**, *9*, 125.
(76) Sotak, C. H.; Hees, P. S.; Huang, H. N.; Hung, M. H.; Krespan, C. G.; Raynolds, S. *Magn. Reson. Med.* **1993**, *29*, 188.
(77) Bartusik, D.; Tomanek, B.; Siluk, D.; Kaliszan, R.; Fallone, G. *Anal. Biochem.* **2009**, *387*, 315.
(78) McNab, J. A.; Yung, A. C.; Kozlowski, P. *Magma* **2004**, *17*, 288.
(79) Duong, T. Q.; Kim, S. G. *Magn. Reson. Med.* **2000**, *43*, 393.
(80) Jacob, R. E.; Chang, Y. V.; Choong, C. K.; Bierhals, A.; Zheng Hu, D.; Zheng, J.; Yablonskiy, D. A.; Woods, J. C.; Gierada, D. S.; Conradi, M. S. *Magn. Reson. Med.* **2005**, *54*, 577.
(81) Ito, Y.; Berkowitz, B. A. *Vision Res.* **2001**, *41*, 1307.
(82) Yu, J. X.; Kodibagkar, V. D.; Cui, W.; Mason, R. P. *Curr. Med. Chem.* **2005**, *12*, 819.
(83) Thulborn, K. R.; Waterton, J. C.; Matthews, P. M.; Radda, G. K. *Biochim. Biophys. Acta* **1982**, *714*, 265.
(84) Ogawa, S.; Lee, T. M.; Kay, A. R.; Tank, D. W *Proc. Natl. Acad. Sci. U.S.A.* **1990**, *87*, 9868.
(85) Di Salle, F.; Formisano, E.; Linden, D. E.; Goebel, R.; Bonavita, S.; Pepino, A.; Smaltino, F.; Tedeschi, G. *Eur. J. Radiol.* **1999**, *30*, 84.
(86) Baudelet, C.; Gallez, B. *Magn. Reson. Med.* **2002**, *48*, 980.
(87) Backer, J. M.; Budker, V. G.; Eremenko, S. I.; Molin, Y. N. *Biochim. Biophys. Acta* **1977**, *460*, 152.
(88) Gurbiel, R.; Cieszka, K.; Pajak, S.; Subczynski, W.; Lukiewicz, S. *Folia Histochem. Cytochem. (Krakow)* **1980**, *18*, 87.
(89) Morse, P. D., 2nd; Swartz, H. M. *Magn. Reson. Med.* **1985**, *2*, 114.
(90) Kusumi, A.; Subczynski, W. K.; Hyde, J. S. *Proc. Natl. Acad. Sci. U.S.A.* **1982**, *79*, 1854.
(91) Subczynski, W. K.; Hyde, J. S. *Biochim. Biophys. Acta* **1981**, *643*, 283.
(92) Thomas, D. D.; Wendt, C. H.; Francisz, W.; Hyde, J. S. *Biophys. J.* **1983**, *43*, 131.
(93) Subczynski, W. K.; Lukiewicz, S.; Hyde, J. S. *Magn. Reson. Med.* **1986**, *3*, 747.
(94) Swartz, H. M.; Clarkson, R. B. *Phys. Med. Biol.* **1998**, *43*, 1957.
(95) Khan, N.; Hou, H.; Hein, P.; Comi, R. J.; Buckey, J. C.; Grinberg, O.; Salikhov, I.; Lu, S. Y.; Wallach, H.; Swartz, H. M. *Adv. Exp. Med. Biol.* **2005**, *566*, 119.
(96) He, J.; Beghein, N.; Clarkson, R. B.; Swartz, H. M.; Gallez, B. *Phys. Med. Biol.* **2001**, *46*, 3323.
(97) Kessel, A. R.; Salimov, V. G. *Russ. Phys. J.* **1971**, *14*, 317.
(98) Teng, C. L.; Hong, H.; Kiihne, S.; Bryant, R. G. *J. Magn. Reson.* **2001**, *148*, 31.
(99) Eastman, M. P.; Kooser, R. G.; Das, M. R.; Freed, J. H. *J. Chem. Phys.* **1969**, *51*, 2690.
(100) Gorter, C. J.; Van Vleck, J. H. *Phys. Rev.* **1947**, *72*, 1128.
(101) Anderson, P. W.; Weiss, P. R. *Rev. Mod. Phys.* **1953**, *25*, 269.
(102) Grinberg, O. Y.; Williams, B. B.; Ruuge, A. E.; Grinberg, S. A.; Wilcox, D. E.; Swartz, H. M.; Freed, J. H. *J. Phys. Chem. B* **2007**, *111*, 13316.
(103) Murugesan, R.; Cook, J. A.; Devasahayam, N.; Afeworki, M.; Subramanian, S.; Tschudin, R.; Larsen, J. A.; Mitchell, J. B.; Russo, A.; Krishna, M. C. *Magn. Reson. Med.* **1997**, *38*, 409.
(104) Ernst, R. R.; Anderson, W. A. *Rev. Sci. Instrum.* **1966**, *37*, 93.
(105) Quine, R. W.; A., R. G.; Eaton, S. S.; Eaton, G. R. *Concepts Magn. Reson.* **2002**, *15*, 59.
(106) Subramanian, S.; Matsumoto, K.; Mitchell, J. B.; Krishna, M. C. *NMR Biomed.* **2004**, *17*, 263.
(107) Oikawa, K.; Ogata, T.; Togashi, H.; Lin, Y.; Sato, T. *Anal. Sci.* **1995**, *11*, 885.
(108) He, G.; Shankar, R. A.; Chzhan, M.; Samouilov, A.; Kuppusamy, P.; Zweier, J. L. *Proc. Natl. Acad. Sci. U.S.A.* **1999**, *96*, 4586.
(109) Rupp, L. W.; Wittig, K. R.; Wash, M. W. *Am. J. Phys.* **1976**, *44*, 655.
(110) Kuppusamy, P.; Chzhan, M.; Vij, K.; Shteynbuk, M.; Lefer, D. J.; Giannella, E.; Zweier, J. L. *Proc. Natl. Acad. Sci. U.S.A.* **1994**, *91*, 3388.
(111) Thomas, S. R.; Busse, L. J.; Scheuck, V. F. *AAPM 1985 Summer School in Medical Physics*; Medical Physics Publishing: Seattle, WA, 1985.
(112) Golay, M. J. *Rev. Sci. Instrum.* **1958**, *29*, 313.
(113) Chzhan, M.; Kuppusamy, P.; Zweier, J. L. *J. Magn. Reson., Ser. B* **1995**, *108*, 67.
(114) He, G.; Petryakov, S.; Samouilov, A.; Chzhan, M.; Kuppusamy, P.; Zweier, J. L. *J. Magn. Reson.* **2001**, *149*, 218.
(115) Froncisz, W.; Hyde, J. S. *J. Magn. Reson.* **1982**, *47*, 515.
(116) Sotgiu, A. *J. Magn. Reson.* **1985**, *65*, 206.
(117) Bacic, G.; Nilges, M. J.; Magin, R. L.; Walczak, T.; Swartz, H. M. *Magn. Reson. Med.* **1989**, *10*, 266.
(118) Chzhan, M.; Shtenbuk, M.; Kuppusamy, P.; Zweier, J. L. *J. Magn. Reson., Ser. A* **1993**, *105*, 49.
(119) Poole, C. P. J. *Electron Spin Resonance: A Comprehensive Treatise on Experimental Techniques*, 2nd ed.; Dover Publications: Mineola, 1997.
(120) Stoner, J. W.; Szymanski, D.; Eaton, S. S.; Quine, R. W.; Rinard, G. A.; Eaton, G. R. *J. Magn. Reson.* **2004**, *170*, 127.
(121) Robinson, B. H.; Mailer, C.; Reese, A. W. *J. Magn. Reson.* **1999**, *138*, 199.
(122) Bales, B. L.; Peric, M.; Lamy-Freund, M. T. *J. Magn. Reson.* **1998**, *132*, 279.
(123) Williams, B. B.; Pan, X.; Halpern, H. J. *J. Magn. Reson.* **2005**, *174*, 88.
(124) Alecci, M.; Colacicchi, S.; Indovina, P. L.; Momo, F.; Pavone, P.; Sotgiu, A. *J. Magn. Reson. Imaging* **1990**, *8*, 59.
(125) Kuppusamy, P.; Wang, P.; Zweier, J. L. *Magn. Reson. Med.* **1995**, *34*, 99.
(126) Deans, S. R. *The Radon Transform and Some of Its Applications*; John Wiley & Sons: New York, 1983.
(127) Herman, G. T.; Lent, A. *Comput. Biol. Med.* **1976**, *6*, 273.
(128) Wang, C. X.; Snydera, W. E.; Bilbro, G.; Santago, P. *Comput. Biol. Med.* **1998**, *28*, 13.
(129) Press, W. H.; Flannery, B. P.; Teukolsky, S. A.; Vetterling, W. T. In *Numerical Recipes in FORTRAN: The Art of Scientific Computing*; Cambridge University Press: Cambridge, 1992.
(130) Maltempo, M. M. *J. Magn. Reson.* **1986**, *69*, 156.
(131) Hanson, K. M. *J. Op. Soc. Am.* **1983**, *73*, 1501.
(132) Epel, B.; Sundramoorthy, S. V.; Mailer, C.; Halpern, H. J. *Concepts Magn. Reson.* **2008**, *33B*, 163.
(133) Mailer, C.; Robinson, B. H.; Williams, B. B.; Halpern, H. J. *Magn. Reson. Med.* **2003**, *49*, 1175.
(134) Williams, B. B.; Hou, H.; Grinberg, O. Y.; Demidenko, E.; Swartz, H. M. *Antioxid. Redox Signaling* **2007**, *9*, 1691.
(135) Dadok, J.; Sprecher, R. F. *J. Magn. Reson.* **1974**, *13*, 243.
(136) Joshi, J. P.; Ballard, J. R.; Rinard, G. A.; Quine, R. W.; Eaton, S. S.; Eaton, G. R. *J. Magn. Reson.* **2005**, *175*, 44.
(137) Lewitt, R. M. *IEEE Proc.* **1983**, *71*, 390.
(138) Kak, A. C.; Slaney, M.; *Principles of Computerized Tomographic Imaging*; IEEE Press: New York, 1988.
(139) Delaney, A. H.; Bresler, Y. *IEEE Trans. Image Process.* **1996**, *5*, 740.
(140) Ahmad, R.; Clymer, B.; Vikram, D. S.; Deng, Y.; Hirata, H.; Zweier, J. L.; Kuppusamy, P. *J. Magn. Reson.* **2007**, *184*, 246.
(141) Tseitlin, M.; Dhami, A.; Eaton, S. S.; Eaton, G. R. *J. Magn. Reson.* **2007**, *184*, 157.
(142) Subramanian, S.; Devasahayam, N.; Murugesan, R.; Yamada, K.; Cook, J.; Taube, A.; Mitchell, J. B.; Lohman, J. A.; Krishna, M. C. *Magn. Reson. Med.* **2002**, *48*, 370.
(143) Deng, Y.; Petryakov, S.; He, G.; Kesselring, E.; Kuppusamy, P.; Zweier, J. L. *J. Magn. Reson.* **2007**, *185*, 283.
(144) Grinberg, O. Y.; Smirnov, A. I.; Swartz, H. M. *J. Magn. Reson.* **2001**, *152*, 247.
(145) Som, S.; Potter, L. C.; Ahmad, R.; Vikram, D. S.; Kuppusamy, P. *J. Magn. Reson.* **2008**, *193*, 210.
(146) Hyde, J. S.; Mchaourab, H. S.; Camenisch, T.; Ratke, J. J.; Cox, R. W.; Froncisz, W. *Rev. Sci. Instrum.* **1998**, *69*, 2622.
(147) Hyde, J. S.; Camenisch, T. G.; Ratke, J. J.; Strangeway, R. A.; Froncisz, W. In *Biomedical EPR, Part B: Methodology, Instrumenta-*

tion, and Dynamics; Eaton, S. R., Eaton, G. R., Berliner, L. J., Eds.; Kluwer Academic/Plenum Publishers: New York, 2005.
(148) Lurie, D. J.; Bussell, D. M.; Bell, L. H.; Mallard, J. R. *J. Magn. Reson.* **1988**, *76*, 366.
(149) Overhauser, A. W. *Phys. Rev.* **1953**, *92*, 411.
(150) Krishna, M. C.; English, S.; Yamada, K.; Yoo, J.; Murugesan, R.; Devasahayam, N.; Cook, J. A.; Golman, K.; Ardenkjaer-Larsen, J. H.; Subramanian, S.; Mitchell, J. B. *Proc. Natl. Acad. Sci. U.S.A.* **2002**, *99*, 2216.
(151) Matsumoto, S.; Yamada, K.; Hirata, H.; Yasukawa, K.; Hyodo, F.; Ichikawa, K.; Utsumi, H. *Magn. Reson. Med.* **2007**, *57*, 806.
(152) Popp, C. A.; Hyde, J. S. *J. Magn. Reson.* **1981**, *43*, 249.
(153) Gallez, B.; Bacic, G.; Goda, F.; Jiang, J.; O'Hara, J. A.; Dunn, J. F.; Swartz, H. M. *Magn. Reson. Med.* **1996**, *35*, 97.
(154) Liu, S.; Timmins, G. S.; Shi, H.; Gasparovic, C. M.; Liu, K. J. *NMR Biomed.* **2004**, *17*, 327.
(155) Smirnov, A. I.; Clarkson, R. B.; Belford, R. L. *J. Magn. Reson., Ser. B* **1996**, *111*, 149.
(156) Liu, K. J.; Gast, P.; Moussavi, M.; Norby, S. W.; Vahidi, N.; Walczak, T.; Wu, M.; Swartz, H. M. *Proc. Natl. Acad. Sci. U.S.A.* **1993**, *90*, 5438.
(157) Ilangovan, G.; Zweier, J. L.; Kuppusamy, P. *J. Phys. Chem. B* **2000**, *104*, 9404.
(158) Pandian, R. P.; Dolgos, M.; Dang, V.; Sostaric, J. Z.; Woodward, P. M.; Kuppusamy, P. *Chem. Mater.* **2007**, *19*, 3545.
(159) Manivannan, A.; Yanagi, H.; Ilangovan, G.; Kuppusamy, P. *J. Magn. Magn. Mater.* **2001**, *233*, L131.
(160) Pandian, R. P.; Parinandi, N. L.; Ilangovan, G.; Zweier, J. L.; Kuppusamy, P. *Free Radical Biol. Med.* **2003**, *35*, 1138.
(161) Vahidi, N.; Clarkson, R. B.; Liu, K. J.; Norby, S. W.; Wu, M.; Swartz, H. M. *Magn. Reson. Med.* **1994**, *31*, 139.
(162) Smirnova, T. I.; Smirnov, A. I.; Clarkson, R. B.; Belford, R. L. *J. Phys. Chem.* **1994**, *98*, 2464.
(163) James, P. E.; Grinberg, O. Y.; Goda, F.; Panz, T.; O'Hara, J. A.; Swartz, H. M. *Magn. Reson. Med.* **1997**, *38*, 48.
(164) Goda, F.; Liu, K. J.; Walczak, T.; O'Hara, J. A.; Jiang, J.; Swartz, H. M. *Magn. Reson. Med.* **1995**, *33*, 237.
(165) Shen, J.; Bottle, S.; Khan, N.; Grinberg, O.; Reid, D.; Micallef, A.; Swartz, H. *Appl. Magn. Reson.* **2002**, *22*, 357.
(166) Dhimitruka, I.; Velayutham, M.; Bobko, A. A.; Khramtsov, V. V.; Villamena, F. A.; Hadad, C. M.; Zweier, J. L. *Bioorg. Med. Chem. Lett.* **2007**, *17*, 6801.
(167) Philipp, R.; McIntyre, J. O.; Robinson, B. H.; Huth, H.; Trommer, W.; Fleischer, S. *Biochim. Biophys. Acta* **1984**, *790*, 251.
(168) Liu, K. J.; Grinstaff, M. W.; Jiang, J.; Suslick, K. S.; Swartz, H. M.; Wang, W. *Biophys. J.* **1994**, *67*, 896.
(169) Glockner, J. F.; Norby, S. W.; Swartz, H. M. *Magn. Reson. Med.* **1993**, *29*, 12.
(170) Halpern, H. J.; Peric, M.; Nguyen, T. D.; Spencer, D. P.; Teicher, B. A.; Lin, Y. J.; Bowman, M. K. *J. Magn. Reson.* **1990**, *90*, 40.
(171) Alecci, M.; Ferrari, M.; Quaresima, V.; Sotgiu, A.; Ursini, C. L. *Biophys. J.* **1994**, *67*, 1274.
(172) Ardenkjaer-Larsen, J. H.; Laursen, I.; Leunbach, I.; Ehnholm, G.; Wistrand, L. G.; Petersson, J. S.; Golman, K. *J. Magn. Reson.* **1998**, *133*, 1.
(173) Elas, M.; Ahn, K. H.; Parasca, A.; Barth, E. D.; Lee, D.; Haney, C.; Halpern, H. J. *Clin. Cancer Res.* **2006**, *12*, 4209.
(174) Kutala, V. K.; Parinandi, N. L.; Pandian, R. P.; Kuppusamy, P. *Antioxid. Redox Signaling* **2004**, *6*, 597.
(175) Subramanian, S.; Yamada, K.; Irie, A.; Murugesan, R.; Cook, J. A.; Devasahayam, N.; Van Dam, G. M.; Mitchell, J. B.; Krishna, M. C. *Magn. Reson. Med.* **2002**, *47*, 1001.
(176) Driesschaert, B.; Charlier, N.; Gallez, B.; Marchand-Brynaert, J. *Bioorg. Med. Chem. Lett.* **2008**, *18*, 4291.
(177) Bobko, A. A.; Dhimitruka, I.; Eubank, T. D.; Marsh, C. B.; Zweier, J. L.; Khramtsov, V. V. *Free Radical Biol. Med.* **2009**, *47*, 654.
(178) Liu, Y.; Villamena, F. A.; Sun, J.; Xu, Y.; Dhimitruka, I.; Zweier, J. L. *J. Org. Chem.* **2008**, *73*, 1490.
(179) Dang, V.; Wang, J.; Feng, S.; Buron, C.; Villamena, F. A.; Wang, P. G.; Kuppusamy, P. *Bioorg. Med. Chem. Lett.* **2007**, *17*, 4062.
(180) Bratasz, A.; Kulkarni, A. C.; Kuppusamy, P. *Biophys. J.* **2007**, *92*, 2918.
(181) Swartz, H. M.; Boyer, S.; Gast, P.; Glockner, J. F.; Hu, H.; Liu, K. J.; Moussavi, M.; Norby, S. W.; Vahidi, N.; Walczak, T.; Wu, M.; Clarkson, R. B. *Magn. Reson. Med.* **1991**, *20*, 333.
(182) Zweier, J. L.; Chzhan, M.; Ewert, U.; Schneider, G.; Kuppusamy, P. *J. Magn. Reson., Ser. B* **1994**, *105*, 52.
(183) Smirnov, A. I.; Norby, S. W.; Clarkson, R. B.; Walczak, T.; Swartz, H. M. *Magn. Reson. Med.* **1993**, *30*, 213.
(184) Swartz, H. M.; Liu, K. J.; Goda, F.; Walczak, T. *Magn. Reson. Med.* **1994**, *31*, 229.
(185) Afeworki, M.; Miller, N. R.; Devasahayam, N.; Cook, J.; Mitchell, J. B.; Subramanian, S.; Krishna, M. C. *Free Radical Biol. Med.* **1998**, *25*, 72.
(186) Ilangovan, G.; Zweier, J. L.; Kuppusamy, P. *J. Phys. Chem. B* **2000**, *104*, 4047.
(187) Turek, P.; Andre, J. J.; Giraudeau, A.; Simon, J. *Chem. Phys. Lett.* **1987**, *134*, 471.
(188) Ilangovan, G.; Li, H.; Zweier, J. L.; Kuppusamy, P. *J. Phys. Chem. B* **2001**, *105*, 5323.
(189) Ilangovan, G.; Manivannan, A.; Li, H.; Yanagi, H.; Zweier, J. L.; Kuppusamy, P. *Free Radical Biol. Med.* **2002**, *32*, 139.
(190) Pandian, R. P.; Dolgos, M.; Marginean, C.; Woodward, P. M.; Hammel, P. C.; Manoharan, P. T.; Kuppusamy, P. *J. Mater. Chem.* **2009**, *19*, 4138.
(191) Pandian, R. P.; Kim, Y. I.; Woodward, P. M.; Zweier, J. L.; Manoharan, P. T.; Kuppusamy, P. *J. Mater. Chem.* **2006**, *16*, 3609.
(192) Dinguizli, M.; Beghein, N.; Gallez, B. *Physiol. Meas.* **2008**, *29*, 1247.
(193) Eteshola, E.; Pandian, R. P.; Lee, S. C.; Kuppusamy, P. *Biomed. Microdevices* **2009**, *11*, 379.
(194) Gallez, B.; Debuyst, R.; Liu, K. J.; Demeure, R.; Dejehet, F.; Swartz, H. M. *Magma* **1996**, *4*, 71.
(195) He, J.; Beghein, N.; Ceroke, P.; Clarkson, R. B.; Swartz, H. M.; Gallez, B. *Magn. Reson. Med.* **2001**, *46*, 610.
(196) Meenakshisundaram, G.; Eteshola, E.; Pandian, R. P.; Bratasz, A.; Lee, S. C.; Kuppusamy, P. *Biomed. Microdevices* **2009**, *11*, 773.
(197) Belanger, M. C.; Marois, Y. *J. Biomed. Mater. Res.* **2001**, *58*, 467.
(198) Pajak, S.; Cieszka, K.; Gurbiel, R.; Subczynski, W. K.; Lukiewicz, S. J. *Third Meeting of the Polish Biophysical Society*; Wroclaw-Olesnicka, 1978; p 70.
(199) Sarna, T.; Duleba, A.; Korytowski, W.; Swartz, H. M. *Arch. Biochem. Biophys.* **1980**, *200*, 140.
(200) Shen, J.; Khan, N.; Lewis, L. D.; Armand, R.; Grinberg, O.; Demidenko, E.; Swartz, H. *Biophys. J.* **2003**, *84*, 1291.
(201) Ashikawa, I.; Yin, J. J.; Subczynski, W. K.; Kouyama, T.; Hyde, J. S.; Kusumi, A. *Biochemistry* **1994**, *33*, 4947.
(202) Subczynski, W. K.; Wisniewska, A.; Yin, J. J.; Hyde, J. S.; Kusumi, A. *Biochemistry* **1994**, *33*, 7670.
(203) Subczynski, W. K.; Markowska, E.; Sielewiesiuk, J. *Biochim. Biophys. Acta* **1991**, *1068*, 68.
(204) Subczynski, W. K.; Lewis, R. N.; McElhaney, R. N.; Hodges, R. S.; Hyde, J. S.; Kusumi, A. *Biochemistry* **1998**, *37*, 3156.
(205) Hockel, M.; Schlenger, K.; Mitze, M.; Schaffer, U.; Vaupel, P. *Semin. Radiat. Oncol.* **1996**, *6*, 3.
(206) Rofstad, E. K. *Int. J. Radiat. Biol.* **2000**, *76*, 589.
(207) Selvendiran, K.; Bratasz, A.; Kuppusamy, M. L.; Tazi, M. F.; Rivera, B. K.; Kuppusamy, P. *Int. J. Cancer* **2009**, *125*, 2198.
(208) Menon, C.; Fraker, D. L. *Cancer Lett.* **2005**, *221*, 225.
(209) Evans, S. M.; Du, K. L.; Chalian, A. A.; Mick, R.; Zhang, P. J.; Hahn, S. M.; Quon, H.; Lustig, R.; Weinstein, G. S.; Koch, C. J. *Int. J. Radiat. Oncol. Biol. Phys.* **2007**, *69*, 1024.
(210) Halpern, H. J.; Yu, C.; Peric, M.; Barth, E.; Grdina, D. J.; Teicher, B. A. *Proc. Natl. Acad. Sci. U.S.A.* **1994**, *91*, 13047.
(211) Halpern, H. J.; Yu, C.; Peric, M.; Barth, E. D.; Karczmar, G. S.; River, J. N.; Grdina, D. J.; Teicher, B. A. *Radiat. Res.* **1996**, *145*, 610.
(212) Ilangovan, G.; Bratasz, A.; Li, H.; Schmalbrock, P.; Zweier, J. L.; Kuppusamy, P. *Magn. Reson. Med.* **2004**, *52*, 650.
(213) Bratasz, A.; Pandian, R. P.; Deng, Y.; Petryakov, S.; Grecula, J. C.; Gupta, N.; Kuppusamy, P. *Magn. Reson. Med.* **2007**, *57*, 950.
(214) Hou, H.; Lariviere, J. P.; Demidenko, E.; Gladstone, D.; Swartz, H.; Khan, N. *Radiother. Oncol.* **2009**, *91*, 126.
(215) Eubank, T. D.; Roberts, R. D.; Khan, M.; Curry, J. M.; Nuovo, G. J.; Kuppusamy, P.; Marsh, C. B. *Cancer Res.* **2009**, *69*, 2133.
(216) Gallez, B.; Debuyst, R.; Dejehet, F.; Liu, K. J.; Walczak, T.; Goda, F.; Demeure, R.; Taper, H.; Swartz, H. M. *Magn. Reson. Med.* **1998**, *40*, 152.
(217) Meenakshisundaram, G.; Eteshola, E.; Pandian, R. P.; Bratasz, A.; Selvendiran, K.; Lee, S. C.; Krishna, M. C.; Swartz, H. M.; Kuppusamy, P. *Biomed. Microdevices* **2009**, *11*, 817.
(218) Gallez, B.; Baudelet, C.; Jordan, B. F. *NMR Biomed.* **2004**, *17*, 240.
(219) Friedman, B. J.; Grinberg, O. Y.; Isaacs, K. A.; Walczak, T. M.; Swartz, H. M. *J. Mol. Cell. Cardiol.* **1995**, *27*, 2551.
(220) Zweier, J. L.; Kuppusamy, P. *Proc. Natl. Acad. Sci. U.S.A.* **1988**, *85*, 5703.
(221) Zweier, J. L.; Thompson-Gorman, S.; Kuppusamy, P. *J. Bioenerg. Biomembr.* **1991**, *23*, 855.
(222) Grinberg, O. Y.; Grinberg, S. A.; Friedman, B. J.; Swartz, H. M. *Adv. Exp. Med. Biol.* **1997**, *411*, 171.
(223) Angelos, M. G. ; Kutala, V. K.; Torres, C. A.; He, G.; Stoner, J. D.; Mohammad, M.; Kuppusamy, P. *Am. J. Physiol. Heart Circ. Physiol.* **2006**, *290.*, H341..
(224) Zhu, X.; Zuo, L.; Cardounel, A. J.; Zweier, J. L.; He, G. *Antioxid. Redox Signaling* **2007**, *9*, 447.

(225) Khan, M.; Mohan, I. K.; Kutala, V. K.; Kotha, S. R.; Parinandi, N. L.; Hamlin, R. L.; Kuppusamy, P. *Antioxid. Redox Signaling* **2009**, *11*, 725.
(226) Khan, M.; Kutala, V. K.; Wisel, S.; Chacko, S. M.; Kuppusamy, M. L.; Kwiatkowski, P.; Kuppusamy, P. *Adv. Exp. Med. Biol.* **2008**, *614*, 45.
(227) Khan, M.; Kutala, V. K.; Vikram, D. S.; Wisel, S.; Chacko, S. M.; Kuppusamy, M. L.; Mohan, I. K.; Zweier, J. L.; Kwiatkowski, P.; Kuppusamy, P. *Am. J. Physiol. Heart Circ. Physiol.* **2007**, *293*, H2129.
(228) Chacko, S. M.; Khan, M.; Kuppusamy, M. L.; Pandian, R. P.; Varadharaj, S.; Selvendiran, K.; Bratasz, A.; Rivera, B. K.; Kuppusamy, P. *Am. J. Physiol. Heart Circ. Physiol.* **2009**, *296*, H1263.
(229) Khan, M.; Meduru, S.; Mohan, I. K.; Kuppusamy, M. L.; Wisel, S.; Kulkarni, A.; Rivera, B. K.; Hamlin, R. L.; Kuppusamy, P. *J. Mol. Cell. Cardiol.* **2009**, *47*, 275.
(230) Gordillo, G. M.; Schlanger, R.; Wallace, W. A.; Bergdall, V.; Bartlett, R.; Sen, C. K. *Methods Enzymol.* **2004**, *381*, 575.
(231) Hopf, H. W.; Gibson, J. J.; Angeles, A. P.; Constant, J. S.; Feng, J. J.; Rollins, M. D.; Zamirul Hussain, M.; Hunt, T. K. *Wound Repair Regener.* **2005**, *13*, 558.
(232) Mills, C.; Bryson, P. *Eur. J. Cardiothorac. Surg.* **2006**, *30*, 153.
(233) Schugart, R. C.; Friedman, A.; Zhao, R.; Sen, C. K. *Proc. Natl. Acad. Sci. U.S.A.* **2008**, *105*, 2628.
(234) Lu, C.; Rollins, M.; Hou, H.; Swartz, H. M.; Hopf, H.; Miclau, T.; Marcucio, R. S. *Iowa Orthop. J.* **2008**, *28*, 14.
(235) James, P. E.; Bacic, G.; Grinberg, O. Y.; Goda, F.; Dunn, J. F.; Jackson, S. K.; Swartz, H. M. *Free Radical Biol. Med.* **1996**, *21*, 25.
(236) Jiang, J.; Nakashima, T.; Liu, K. J.; Goda, F.; Shima, T.; Swartz, H. M. *J. Appl. Physiol.* **1996**, *80*, 552.
(237) Glockner, J. F.; Chan, H. C.; Swartz, H. M. *Magn. Reson. Med.* **1991**, *20*, 123.
(238) Hou, H.; Grinberg, O.; Williams, B.; Grinberg, S.; Yu, H.; Alvarenga, D. L.; Wallach, H.; Buckey, J.; Swartz, H. M. *Physiol. Meas.* **2007**, *28*, 963.
(239) Liu, K. J.; Bacic, G.; Hoopes, P. J.; Jiang, J.; Du, H.; Ou, L. C.; Dunn, J. F.; Swartz, H. M. *Brain Res.* **1995**, *685*, 91.

CR900396Q